OCTOBER 2009 VOL 2 NO 10
www.nature.com/naturegeoscience

nature geoscience

Wenchuan quake breaks the barriers

SINKING DELTAS
Human interference

ARCHAEAN OXYGEN
Nitrogen gives clues

OVERTURNING OZONE
Warming-induced flux

ARTICLES
PUBLISHED ONLINE: 27 SEPTEMBER 2009 | DOI: 10.1038/NGEO636
nature geoscience

Slip maxima at fault junctions and rupturing of barriers during the 2008 Wenchuan earthquake

Zheng-Kang Shen[1,2,3]*, Jianbao Sun[1], Peizhen Zhang[1], Yongge Wan[4], Min Wang[1], Roland Bürgmann[5], Yuehua Zeng[6], Weijun Gan[1], Hua Liao[7] and Qingliang Wang[8]

The disastrous 12 May 2008 Wenchuan earthquake in China took the local population as well as scientists by surprise. Although the Longmen Shan fault zone—which includes the fault segments along which this earthquake nucleated—was well known, geologic and geodetic data indicate relatively low (<3 mm yr^{-1}) deformation rates. Here we invert Global Positioning System and Interferometric Synthetic Aperture Radar data to infer fault geometry and slip distribution associated with the earthquake. Our analysis shows that the geometry of the fault changes along its length: in the southwest, the fault plane dips moderately to the northwest but becomes nearly vertical in the northeast. Associated with this is a change in the motion along the fault from predominantly thrusting to strike-slip. Peak slip along the fault occurs at the intersections of fault segments located near the towns of Yingxiu, Beichuan and Nanba, where fatalities and damage were concentrated. We suggest that these locations represent barriers that failed in a single event, enabling the rupture to cascade through several fault segments and cause a major moment magnitude (M_w) 7.9 earthquake. Using coseismic slip distribution and geodetic and geological slip rates, we estimate that the failure of barriers and rupture along multiple segments takes place approximately once in 4,000 years.

The 12 May 2008 Wenchuan earthquake was the largest seismic event in China in more than 50 years. It devastated cities along the northwest margin of the Sichuan basin (Fig. 1), causing fatalities of more than 80,000 (ref. 1). The earthquake occurred on the Longmen Shan fault zone, which is predominantly a convergent zone with a dextral component, separating the Sichuan basin from the eastern margin of the Tibetan plateau[2]. Three major subparallel faults have been mapped to constitute the northeast trending Longmen Shan fault zone: the Pengguan fault (PGF) is to the east along the mountain front, about 10–15 km to its west lies the Beichuan fault (BCF) and the Wenchuan–Maowen fault lies about another 30 km west of the BCF (Fig. 1; ref. 3). All of the faults are northwest dipping, with the BCF and PGF converging into the same ramp system in the mid-crust[2–5]. Field geological studies found evidence of Holocene activity at least for the central PGF and BCF (refs 6–9). The geological-fault slip-rate estimates, however, are fairly low, about 0.3–0.6 mm yr^{-1} of reverse and ~1.0 mm yr^{-1} dextral faulting for the BCF, and 0.2 mm yr^{-1} reverse faulting for the PGF, averaged over the past ~10,000 years (ref. 10). Such low slip rates are consistent with Global Positioning System (GPS) estimates of the shortening rate across the Longmen Shan range of <3 mm yr^{-1} (refs 11, 12) or 1.5±1.0 mm yr^{-1} (ref. 13).

Seismological studies indicate that the Wenchuan mainshock started on the BCF about 30 km southwest of Yingxiu, and propagated unilaterally northeastward[14]. Surface breaks are found along both the BCF and PGF (refs 3, 15–17). The BCF branches into two segments east of Yingxiu, where the primary segment strikes southwestward and the other strand strikes westward through Yingxiu (Fig. 1). Both segments ruptured during the earthquake, and the largest surface slip of ~6.2 m vertical and ~4.5 m dextral motion is found along a ~20 km stretch of the fault northeast of the branching point[3]. There were no mapped fault surface breaks for ~7 km northeast of this 20 km stretch, beyond which rupture was observed along two conjugate segments, one along the primary BCF trending northeast, and the other (the Xiaoyudong segment) trending southeast and connecting to the PGF (Fig. 1). Another peak of coseismic surface offsets on the BCF is found near Beichuan, with 6.5 m vertical and 2.5 m dextral motion, respectively[3]. It is located at a fault juncture, where the BCF bends ~25° clockwise and almost intersects with the Wenchuan–Maowen fault. Yingxiu and Beichuan suffered from the greatest fatalities (~7,700 deaths at Yingxiu with a population of about 12,000 (ref. 18), and ~5,500 deaths at Beichuan with a population of less than 20,000; ref. 19) and most severe structural damage in the earthquake. The maximum surface offset along the PGF is ~3.5 m, mainly in the vertical component[3].

The surface breaks along the BCF trace from ~20 km southwest of Yingxiu (30.95° N, 103.45° E) to ~10 km southwest of Qingchuan (32.50° N, 105. 20° N), for a total length of ~235 km (ref. 3). Aftershocks, however, extend beyond both ends of the surface rupture for another 55 and 30 km, respectively (Fig. 1). This suggests that a significant portion of the fault rupture did not break to the surface at both ends, and the rupture could be as long as ~320 km. Seismic moment released during the mainshock was measured at 7.6×10^{20} N m by the United States Geological Survey, corresponding to $M_w = 7.9$ (ref. 20). Teleseismic studies indicate unilateral propagation along a 280-km-long rupture, with two slip maxima of about 9 m at ~10 km

[1]State Key Laboratory of Earthquake Dynamics, Institute of Geology, China Earthquake Administration, PO Box 9803, Beijing 100029, China, [2]Department of Geophysics, School of Earth and Space Sciences, Peking University, Beijing 100871, China, [3]Department of Earth and Space Sciences, University of California, Los Angeles, California 90095-1567, USA, [4]College of Disaster Prevention Science and Technology, Yanjiao, Sanhe, Hebei 101601, China, [5]Department of Earth and Planetary Science, University of California, Berkeley, California 94720-4767, USA, [6]Golden Office, US Geological Survey, Colorado 80401, USA, [7]Sichuan Seismological Bureau, Chengdu 610041, China, [8]Second Monitoring Center, China Earthquake Administration, Xi'an 710054, China. *e-mail: zshen@ies.ac.cn; zshen@ucla.edu.

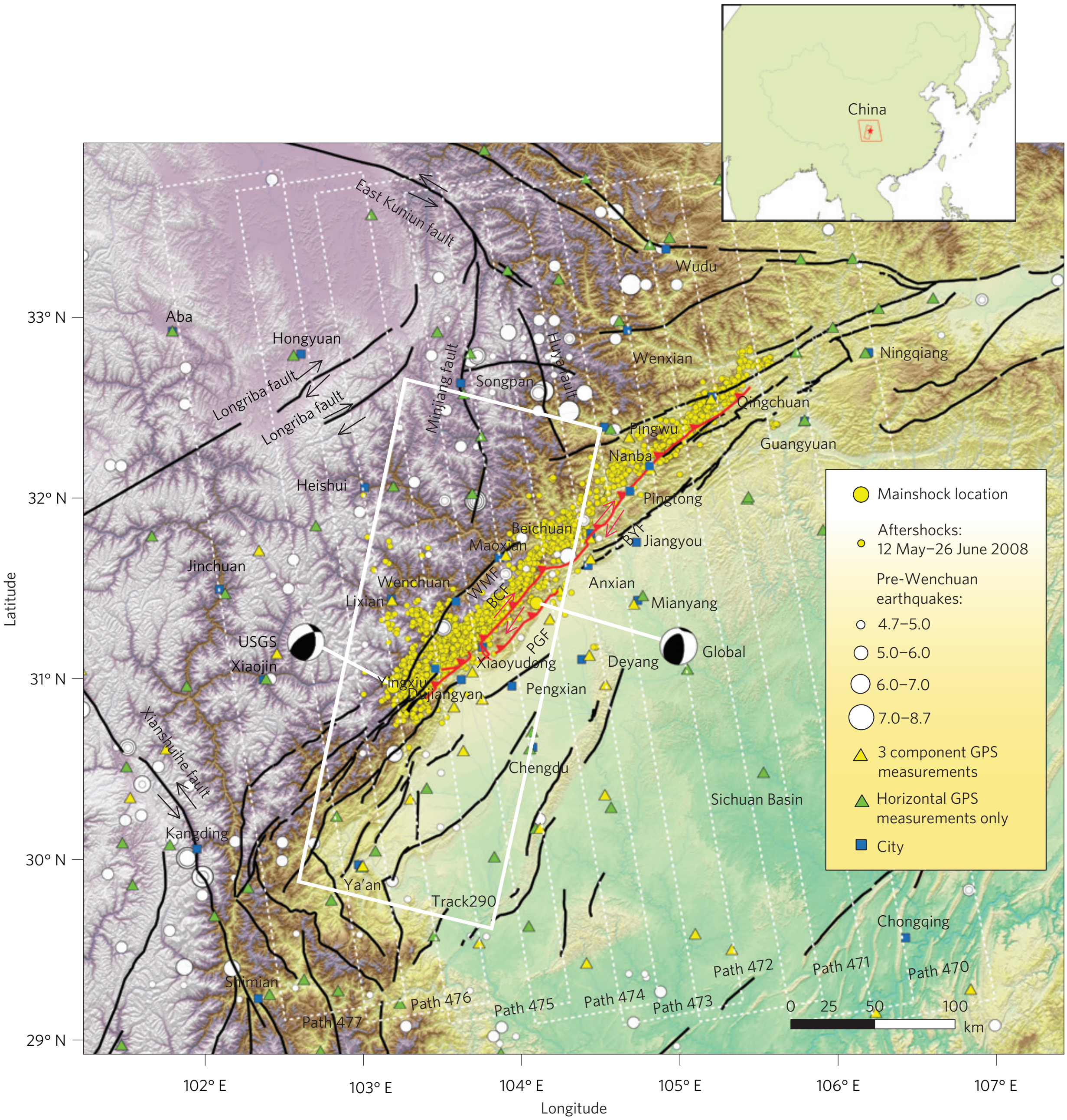

Figure 1 | Tectonic setting of the Wenchuan earthquake. The study region covered by the InSAR images is depicted in the inset map. The areas covered by ALOS (with phased-array-type L-band synthetic aperture radar (PALSAR) sensor) paths 470–477 and Envisat satellite (with Advanced Synthetic Aperture Radar (ASAR) sensor) track 290 are shown as white dashed and white solid rectangles respectively. Black and red lines indicate regional faults and surface traces of coseismic rupture[3]. Green and yellow triangles denote GPS stations whose horizontal-only and horizontal+vertical coseismic offsets are used, respectively. Two mainshock focal mechanism solutions are from United States Geological Survey and Global CMT, respectively. The white and yellow circles show $M > 4.7$ earthquakes of the past century and the Wenchuan aftershocks, respectively. WMF, Wenchuan–Maowen fault.

depth between Yingxiu and Wenchuan and between Beichuan and Pingtong, respectively[14].

Coseismic deformation observed using GPS and InSAR

In this study we use GPS data collected and processed by our group and others and Interferometric Synthetic Aperture Radar (InSAR) measurements from the Advanced Land Observation Satellite (ALOS) and Envisat satellites (see the Methods section) to constrain the geometry and slip distribution of a coseismic rupture model. Only small amounts of postseismic deformation are included in the surface displacement measurements (see the Methods section). The largest coseismic displacement observed by GPS (2.4 m west-northwestward horizontal motion and 0.68 m downward vertical motion, respectively), is measured at a site located near Beichuan on the footwall side and about 2 km from the surface rupture (Fig. 2a). Amplitudes of the displacements are reduced to ~0.1 m about 80 km from the fault. The InSAR interferograms show a total of ~0.7 m range change with L-band SAR data on either side of the fault, although missing near-field data on the hanging-wall side resulted in incomplete coverage of the total range change there. The geometry of the Wenchuan earthquake rupture on the BCF and PGF is complex. Field observations suggest that the faults have varying dip angles, with relatively shallow dip angles along the southwestern section of

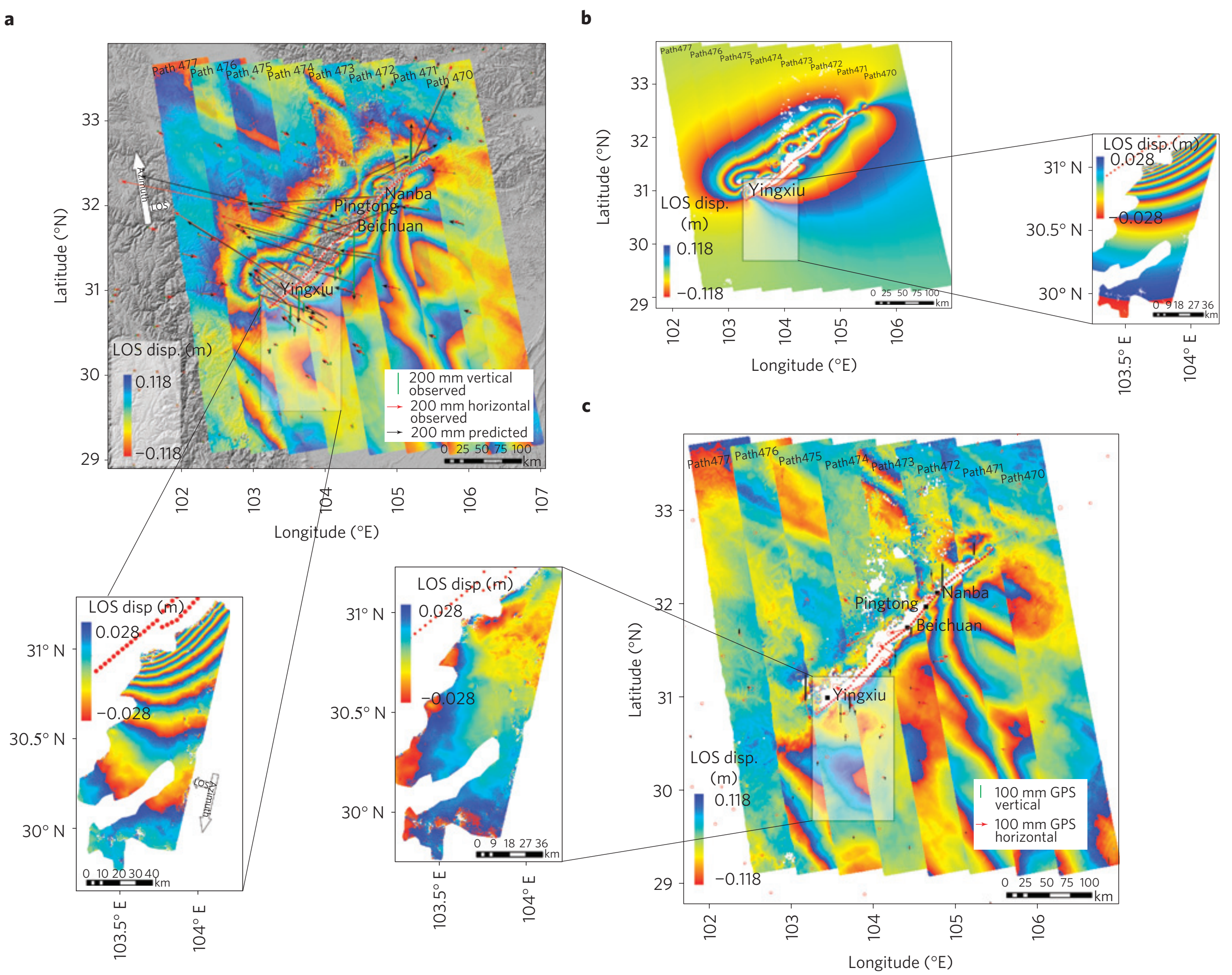

Figure 2 | InSAR and GPS data fittings. a, InSAR range-change data. The white curves depict traces of fault surface breaks, and the red dots show surface points of fault-model patches. Red arrows and green bars are GPS-observed coseismic offsets for the horizontal and vertical components. Black arrows are model-predicted coseismic offsets, horizontal or vertical. **b**, Model-predicted range changes for PALSAR and ASAR measurements. **c**, GPS and InSAR data postfit residuals. Red arrows and black columns are for the horizontal and vertical components of GPS displacements, whose uncertainties are represented as ellipses and lines at arrow and bar tips at 95% confidence.

the rupture and near vertical towards the northeastern[3]. However, dip angles measured at the surface offsets are often highly uncertain and may not reflect the dip angles at depth[3]. Precisely located aftershock hypocenters using the double-differencing method do not clearly illuminate the subsurface rupture geometry either[21]. We therefore simultaneously invert for the first-order fault geometry and the slip distribution on the fault plane in our geodetic inversion.

Fault geometry and slip distribution modelling

Our inversion finds that the BCF dips to the northwest at a moderate angle of ∼43° at the southwest end, and the fault plane gradually becomes steeper northeastward along strike, reaching ∼50° at Nanba (Fig. 3a). The dip angle jumps to ∼56° across the Nanba step-over, and increases progressively to near vertical at the northeast end of the rupture. The PGF dips shallowly at ∼28°, suggesting a common root shared with the Yingxiu–Beichuan segment of the BCF at a depth of ∼18 km, a result consistent with balanced geologic cross-sections across the southern BCF (ref. 22).

The slip distribution on the BCF shows three high-slip concentrations (Fig. 3b–d). The first one is from Yingxiu to Xiaoyudong (subsegment B10 in Fig. 3b) at 0–10 km depth. Its thrust slip averages ∼5 m, and peaks at the surface at 5.8 m. The dextral slip is also concentrated near the surface, with a maximum of about 2.5 m. A second, smaller high-slip area at 0–7 km depth near Beichuan (subsegment B6 in Fig. 3b) has comparable peak slip values, with 5.2 m and 4.8 m of thrust and dextral slip, respectively. In addition to the two prominent high-slip areas, a minor peak is located near Nanba (subsegment B4 in Fig. 3b), where the dextral and reverse slips at the surface reach local maxima of 3.0 m and 3.2 m, respectively.

The three areas of high-slip concentration are located near the intersections of fault segments. The slip maxima close to Yingxiu and Beichuan are near fault bifurcations and conjugates rupture junctions (Fig. 1), and the high slip close to Nanba spans a fault step-over, across which there is a change of fault dip angle. We therefore hypothesize that the Wenchuan earthquake broke through several high-slip junctions that connect major fault segments in a cascade rupture. These connecting structures may represent barriers that rarely fail, and would fail only when high stress has accumulated after multiple rounds of smaller events broke the adjoining individual segments. Such a cascade-rupture scenario helps explain why Yingxiu, Beichuan and Nanba experienced the highest shaking intensity of XI

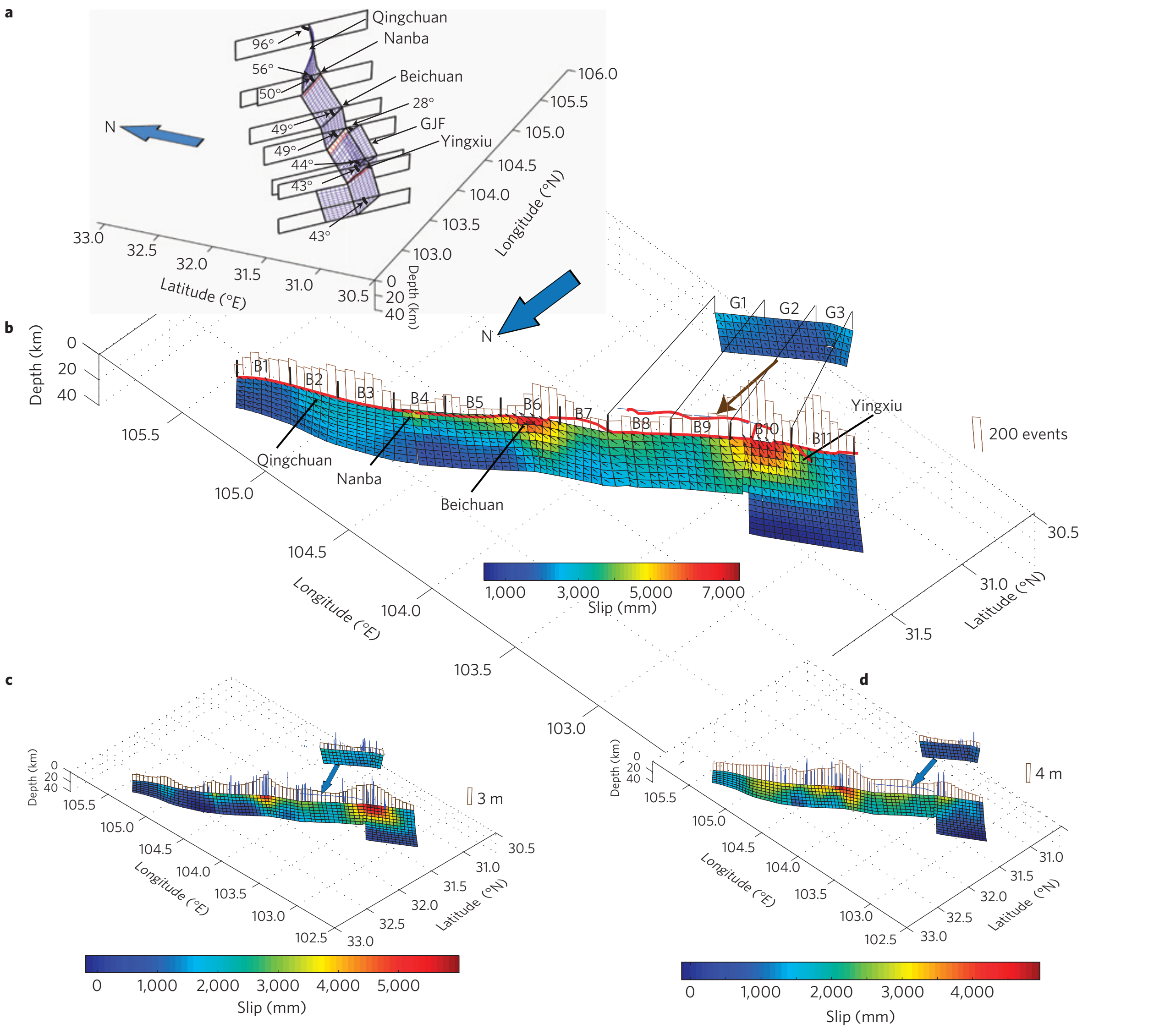

Figure 3 | Inversion results. a, Fault geometry viewed from the southwest, at 45° elevation angle. Six dip angles at fault nodal points marked with an asterisk are inverted for in the solution. **b**, Coseismic slip distribution viewed from the northwest, at 45° elevation angle. The PGF is plotted away from its actual location (whose surface trace is marked here and in **c** and **d** as a blue line). Black arrows show the slip vectors on the fault patches, whose amplitudes are denoted by the patch colour. Red lines are the mapped traces of surface breaks[3]. The brown columns show the density of aftershocks along the fault within 50 km of the surface trace. B1–B11 and G1–G3 are fault subsegments on the BCF and PGF, respectively. **c**,**d**, Reverse and dextral slip amplitudes. The brown columns denote the modelled surface offsets, in comparison with the field observations, shown as blue bars.

and suffered the greatest damage among all the towns located along the fault zone[23].

Moderate amounts of slip are detected along the PGF, with about 1.5 m and 0.7 m of average thrust and dextral motions and peak values of ~2.0 m thrust and 1.5 m dextral slip near its northeast corner close to the surface (Fig. 3). These results agree with geologically measured average surface offsets[3].

Our result also demonstrates moderate amounts of slip on the shallowly dipping fault segment extending northwestward from down-dip of the southwest segment of the BCF (subsegment B10 in Fig. 3b). Peak values of thrust motion reach ~2.0 m close to the hinge connecting to the southwest segment of the BCF. Model inversions without this deep extension produced mechanically implausible results and fit the data significantly worse (see Supplementary Note S1). We conclude that reverse faulting occurred not only on the steep part of the ramp close to the surface but also on a down-dip, near-horizontal detachment fault plane, located up to 30 km away from the surface break.

To estimate the seismic moment release of the fault rupture we integrate the thrust and dextral components along strike and down-dip assuming a shear modulus of 3×10^{10} Pa, and obtain the total seismic moment release of 8.03×10^{20} N m, equivalent to an event of M_w 7.93. This estimate, however, includes a minor contribution from postseismic deformation, because the postearthquake GPS and InSAR measurements were observed with some delays (from days to weeks). Assuming that coseismic and postseismic slips were in the upper and mid-crust respectively and separated at the depth of 20 km (suggested by the lower bound of aftershock depth range[21]), we determine the coseismic moment release above this depth as 7.30×10^{20} N m, equivalent to an event of M_w 7.91. Ongoing analysis of continuous GPS measurements during the early postseismic period[24] supports this first-order correction (see Supplementary Note S2).

The surface slip distribution of our model agrees qualitatively with the dextral (Fig. 3d) and vertical (Fig. 3c) components of field measurements. In particular, both the locations and values

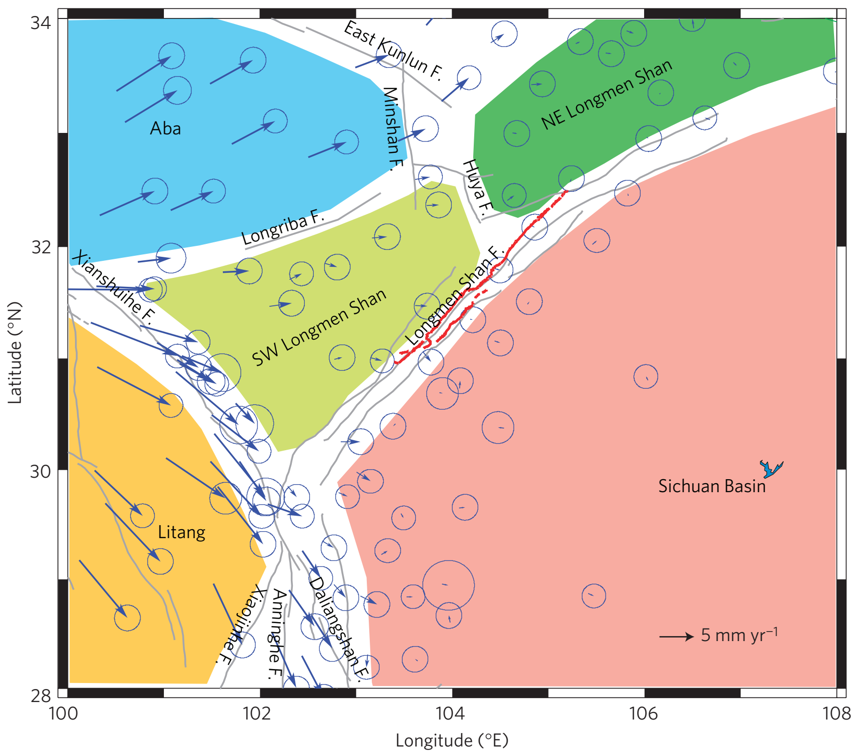

Figure 4 | Secular block-motion model. GPS velocities are referenced to the Sichuan Basin (that is, also the south China block). Error ellipses represent 70% confidence. Coloured regions denote block domains, within which the GPS site velocities are used to define the block motions. Red lines are the surface breaks of the Wenchuan earthquake[6]. Regional faults (grey lines) are modified from ref. 28.

of the peaks of vertical motions match the surface rupture offsets measured by field geologists[3]. Our slip distribution also agrees qualitatively with those derived using teleseismic data[14,25], with twin peaks of slip near Yingxiu and Beichuan. Solutions of Ji and Hayes[14], Wang *et al.*[25], and Zhang *et al.*[26] yielded larger maximum slip, ~9 m, ~12 m, and ~7 m respectively, than ours of 5–6 m, but lie at ~10–20 km depth. The difference may be due to stronger smoothing used in our model and limited depth resolution in the teleseismic studies. A recent slip-distribution model constrained using ALOS InSAR data[27], however, offered similar peak-slip locations to ours, although further details of the slip distributions are different owing to differences in data, fault geometry and smoothing constraints.

The two peaks of fault slip on subsegments B6 and B10 coincide with the locations of dense aftershock populations, suggesting strong local stress concentrations and slip on nearby faults triggered by the large coseismic slip (Fig. 3b). High aftershock concentrations on subsegments B2 and B3 in Fig. 3b between Nanba and Qingchuan coincide with moderate amounts of broadly distributed slip from the surface down to ~20 km depth. The aftershock density is considerably lower along the fault segment between Beichuan and Nanba (subsegment B5 and south part of subsegment B4) than along the neighbouring segments to the northeast and southwest, and the fault slip seems concentrated at shallow depths of less than 8 km, leaving a slip gap on the deeper part of the fault.

Regional block motion and earthquake recurrence interval

What causes the change of faulting mechanism from predominantly thrust in the southwest to dextral in the northeast? To examine how strain is partitioned in the region we devise a block-motion model constrained using regional pre-earthquake GPS velocities (Fig. 4). Our result suggests that, for the region between the East Kunlun fault to the north and the Xianshuihe fault to the south, deformation is partitioned into $4.4 \pm 0.8\,\mathrm{mm\,yr^{-1}}$ dextral slip across the Longriba fault, $1.4 \pm 0.6\,\mathrm{mm\,yr^{-1}}$ convergence and $1.7 \pm 0.6\,\mathrm{mm\,yr^{-1}}$ dextral slip across the central section of the Longmen Shan fault and $1.0 \pm 0.8\,\mathrm{mm\,yr^{-1}}$ convergence across the Minjiang–Huya fault system. Deformation across the northeast section of the Longmen Shan fault is rather minor, mainly in the form of dextral slip ($0.8 \pm 0.6\,\mathrm{mm\,yr^{-1}}$) instead of normal convergence ($0.3 \pm 0.6\,\mathrm{mm\,yr^{-1}}$). Our kinematic model is consistent with the regional topography, which shows sharp contrasts across the southwest-central Longmen Shan fault zone and the Minjiang–Huya fault system, whereas a gentler gradient is found across the northeast section of the Longmen Shan[2] (Fig. 1). More discussions about the regional tectonics and implications of our results can be found in Supplementary Note S3.

We use our results of coseismic slip and secular deformation rates to estimate earthquake recurrence intervals for individual segments of the Longmen Shan fault. We divide the BCF and PGF into 11 and three subsegments, respectively, as shown in Fig. 3b. The faults are assumed to be listric at depth, such that the fault slips interseismically across a flat fault plane at its down-dip continuation, at a rate close to the GPS-measured far-field relative motion. The coseismic slip at the surface, therefore, would be equivalent to the slip deficit accumulated interseismically at the down-dip slip rate. We first take averages within each subsegment of the strike-slip and dip-slip components of coseismic slip over the top five rows of patches, representing the seismogenic part of the crust. We then use the two slip components to obtain the amplitude of the mean coseismic slip within each subsegment.

For each fault subsegment the earthquake recurrence interval T can be estimated as $T = S/V$, where S is the mean coseismic slip on the fault subsegment and V is the secular fault slip (or slip deficit) rate. We use our coseismic slip and both the interseismic block model results and geologic slip rates of individual faults[10] to estimate earthquake recurrence intervals on individual fault subsegments. Results are listed in Table 1. The GPS-derived fault

Table 1 | Earthquake recurrence intervals of fault subsegments.

No.	Fault subsegment area	Coseismic dextral slip	Coseismic reverse slip	Coseismic slip amplitude	Secular dextral rate (GPS, Geol)	Secular reverse rate (GPS, Geol)	Secular rate (GPS, Geol)	Recurrence time (GPS, Geol)
	km^2	m	m	m	mm yr^{-1}	mm yr^{-1}	mm yr^{-1}	10^3 years
BCF 1	400	1.6	1.0	1.9	0.8, /	0.3, /	0.8, /	2.3, /
BCF 2	349	2.2	1.5	2.7	0.8, /	0.3, /	0.8, /	3.3, /
BCF 3	405	2.8	0.5	2.8	0.8, /	0.3, /	0.8, /	3.5, /
BCF 4	399	2.2	1.7	2.8	0.8, /	0.3, /	0.8, /	3.5, /
BCF 5	429	2.7	1.8	3.2	0.8, /	0.3, /	0.8, /	4.0, /
BCF 6	419	3.3	3.5	4.8	1.7, 1.0	1.4, 0.3-0.6	2.2, 1.2	2.2, 4.0
BCF 7	367	2.6	2.5	3.6	1.7, 1.0	1.4, 0.3-0.6	2.2, 1.2	1.6, 3.0
BCF 8	499	2.4	2.6	3.5	/, 1.0	/, 0.3-0.6	/, 1.2	/, 2.9
BCF 9	434	2.2	2.9	3.6	/, 1.0	/, 0.3-0.6	/, 1.2	/, 3.0
BCF 10	456	2.2	4.9	5.3	/, 1.0	/, 0.3-0.6	/, 1.2	/, 4.4
BCF 11	475	1.3	2.7	3.1	1.7, 1.0	1.4, 0.3-0.6	2.2, 1.2	1.4, 2.5
PGF 1	372	0.8	2.0	2.1	/, 0.2	/, 0	/, 0.2	/, 10.0
PGF 2	373	0.7	1.6	1.7	/, 0.2	/, 0	/, 0.2	/, 8.7
PGF 3	263	0.9	1.9	2.1	/, 0.2	/, 0	/, 0.2	/, 10.0
B8 + P1	499	3.0	4.0	5.0	1.7, /	1.4, /	2.2, /	2.3, /
B9 + P2	434	2.8	4.3	5.1	1.7, /	1.4, /	2.2, /	2.3, /
B10 + P3	456	2.7	5.9	6.5	1.7, /	1.4, /	2.2, /	3.0, /

slip rates tend to be greater than geological estimates, because GPS results account for contributions from all of the faults in the region, whereas geological estimates account for contributions only from measured individual faults. Therefore, using GPS estimated fault slip rates tends to produce smaller estimates of recurrence interval than using geological estimates. Nevertheless our analysis yields >1,000 year recurrence intervals for all the fault segments. They are 2.3–4.0 × 10^3 years for the northeast section of the BCF (subsegments B1–B5) and 1.4–4.4 × 10^3 years for the central section of the BCF (segments B6–B11), regardless of whether the characteristic events are assumed to break the BCF only or both the BCF and PGF. The recurrence intervals on the PGF could be as large as 10^4 years. The numbers are 4.0 × 10^3 years and 4.4 × 10^3 years for the Beichuan (B6) and Yingxiu (B10) subsegments if the geological slip rate of the BCF is adopted for the estimates, suggesting the longest recurrence intervals for the two asperity subsegments on the BCF.

In conclusion, we find that the Wenchuan earthquake consecutively ruptured multiple fault segments along the BCF, as well as the subparallel PGF. Fault slip on the BCF was predominantly reverse faulting on shallowly dipping fault segments in the southwest, and changed progressively to predominantly dextral faulting on steeper fault segments as the rupture propagated northeastward. This change in geometry and slip is consistent with a southwest-to-northeast transition from more rapid and mostly convergent to slower and nearly transform motion along the Longmen Shan deduced from a block model of pre-earthquake GPS velocities. The quake produced peak slips near junctures of fault segments, suggesting that these fault junctions represent barriers that rarely fail, recurring as parts of major cascade ruptures about every 4 × 10^3 years. The three major high-slip junctions are near Yingxiu, Beichuan and Nanba, which suffered the highest structural damage and fatality rates among all the towns located along the fault rupture zone.

Methods

GPS and InSAR data and their processing. The GPS data are obtained by the Working Group of the Crustal Motion Observation Network of China Project[29] (with major contributions from members of our group), using data collected before and after the quake in the vicinity of the seismic region. The data are processed using the GAMIT/GLOBK (ref. 30) and QOCA (ref. 31) software. Further details about the determination of coseismic offsets and consideration of postseismic contributions to the measurements are detailed in Supplementary Notes S4 and S2.

Two kinds of SAR data are used to retrieve the coseismic signals of the Wenchuan earthquake, namely Envisat ASAR data in the C-band (5.6 cm wavelength) from ESA and ALOS PALSAR data in the L-band (23.6 cm wavelength) from JAXA. PALSAR data from eight paths (470–477) and eight frames (580–650) are processed, covering a region of ∼540 km wide from west to east and ∼525 km long from south to north, enclosing the entire fault rupture zone (Fig. 1, Supplementary Table S1). The epochs of postseismic PALSAR observations are within 1–7 weeks of the quake (see Supplementary Table S1), and the postseismic deformation accumulated within this time period is found to be small (a few per cent compared with the coseismic signals, see Supplementary Note S2). Details about the data processing and subsampling procedures can be found in Supplementary Note S4, and Supplementary Note S5 provides further information on how the relative weights of the GPS and InSAR data are considered in the model inversions.

Inversion of fault-rupture model. To construct the fault-rupture model we let all fault segments extend to the Earth's surface, including sections where no surface slip was observed. The surface traces of the faults are based on amplitude pixel offsets of SAR image pairs, with additional *a priori* information on fault geometry coming from distribution of aftershocks as described in Supplementary Note S6. Three sections of the fault rupture are defined in the model (Fig. 3): the main fault rupture on BCF, the secondary rupture on PGF, and a blind thrust branching westward from the down-dip end of the southwest segment of BCF. See Supplementary Method S1 for fault meshing and smoothing. We use a Newtonian nonlinear inversion procedure to solve for the fault geometry and slip distribution on faults. The fits of the coseismic slip model to the InSAR and GPS data are shown in Fig. 2. Supplementary Note S7 and Tables S2 and S3 provide further details on the fault slip model, the nonlinear inversion method and results.

Block-motion model. Our interseismic block-motion model is derived from synthesizing four epochs of campaign-mode measurements of the CMONOC project 1999–2007 (refs 32, 33). (Our results should be more precise than estimates of previous studies, because adding the 2007 epoch extends the time span of the CMONOC campaign data from 5 to 8 years compared with our previously published dataset in ref. 34). Assuming rigid blocks for the Sichuan Basin, southwest Longmen Shan, northeast Longmen Shan, Aba and Litang blocks, we estimate the angular velocity of each block with respect to the Sichuan Basin, which seems to be stable with respect to the larger South China microplate[12]. Using the block-rotation parameters we determine the relative displacement rates across the block boundaries, which provides geodetic fault slip-rate estimates and their uncertainties, taking into account all the variance/covariance among different station velocity components (Fig. 4).

Derivation of earthquake recurrence intervals on faults. For those BCF and PGF subsegments (B8–B10 and G1–G3) that are sub-parallel and ruptured together during this quake, quantification of the characteristic event's slip and the fault secular slip rate on the segment becomes less clear. If the Wenchuan earthquake is considered 'characteristic', that is, the largest events would always produce simultaneous rupture on both faults, the recurrence interval on a pair of the fault segments can then be estimated using a sum of the mean slip (weighted over the rupture areas) on the faults and the secular block motion rate relevant to the fault patch. If, however, the Wenchuan earthquake is only a rare occasion, and most of the time rupture would occur on individual faults alone, the recurrence intervals on these fault segments will then have to be estimated separately using their coseismic slips (assuming slips on both faults are 'characteristic') and secular slip rates of individual faults. Owing to limited spatial coverage of the regional GPS network, our block-motion model derived using GPS data does not have the details to differentiate individual fault slip rates from their aggregated rate. We instead use geologically estimated fault slip rates[10] to make the estimation. The corresponding uncertainties of the earthquake recurrence interval estimations are discussed in Supplementary Note S8.

Received 26 January 2009; accepted 21 August 2009; published online 27 September 2009

References

1. http://www.gov.cn/xxgk/pub/govpublic/mrlm/200805/t20080530_32846.html.
2. Burchfiel, B. C. *et al.* A geological and geophysical context for the Wenchuan earthquake of 12 May 2008, Sichuan, People's Republic of China. *GSA Today* **18,** 4–11 (2008).
3. Xu, X. *et al.* Coseismic reverse- and oblique-slip surface faulting generated by the 2008 M_w 7.9 Wenchuan earthquake, China. *Geology* **37,** 515–518 (2009).
4. Burchfiel, B. C., Chen, Z., Liu, Y. & Royden, L. H. Tectonics of the Longmen Shan and adjacent regions. *Int. Geol. Rev.* **37,** 661–735 (1995).
5. Jia, D. *et al.* Longmen Shan fold-thrust belt and its relation to the western Sichuan Basin in central China: New insights from hydrocarbon exploration. *AAPG Bull.* **90,** 1425–1447 (2006).
6. Densmore, A. L. *et al.* Active tectonics of the Beichuan and Pengguan faults at the eastern margin of the Tibetan Plateau. *Tectonics* **26,** TC4005 (2007).
7. Chen, G.-G. *et al.* Primary research of the activity segmentation of Longmenshan fault zone since late Quaternary (in Chinese). *Seismol. Geol.* **29,** 657–673 (2007).
8. Li, C., Song, F. & Ran, Y. Late Quaternary activity and age constraint of the northern Longmenshan Fault Zone (in Chinese). *Seismol. Geol.* **26,** 248–258 (2004).
9. Li, Y., Zhou, R., Densmore, A. L. & Ellis, M. A. Geomorphic evidence for the late Cenozoic strike slipping and thrusting in Longmen mountain at the eastern margin of the Tibetan plateau (in Chinese). *Quat. Res.* **26,** 40–51 (2006).
10. Ma, B. *et al.* Late Quaternary slip rate in the central part of the Longmenshan Fault Zone from terrace deformation along the Minjiang River (in Chinese). *Seismol. Geol.* **27,** 234–242 (2005).
11. Chen, Z. *et al.* Global Positioning System measurements from eastern Tibet and their implications for India/Eurasia intercontinental deformation. *J. Geophys. Res.* **105,** 16215–16227 (2000).
12. Shen, Z.-K., Lu, J., Wang, M. & Burgmann, R. Contemporary crustal deformation around southeast borderland of Tibetan plateau. *J. Geophys. Res.* **110,** B11409 (2005).
13. Wang, Y. *et al.* GPS-constrained inversion of present-day slip rates along major faults of the Sichuan-Yunnan region, China. *Sci. China Ser. D* **51,** 1267–1283 (2008).
14. Ji, C. & Hayes, G. Preliminary result of the May 12, 2008 M_w 7.9 eastern Sichuan, China earthquake, US Geol. Surv., Va.; available at <http://earthquake.usgs.gov/eqcenter/eqinthenews/2008/us2008ryan/finite_fault.php>.
15. Zhang, Z. *et al.* Co-seismic ruptures of the 12 May 2008 M_w 8.0 Wenchuan earthquake, Sichuan: EW crustal shortening on oblique, parallel thrusts along the eastern edge of Tibet. *Eos* **89,** Fall Meet. Suppl., abstr. U23B-0054 (2008).
16. Li, H. *et al.* The M_w 7.9 Wenchuan earthquake of 12 May 2008, Sichuan, China: Surface rupture and oblique right-lateral coseismic thrusting. *Eos* **89,** Fall Meet. Suppl., abstr. T33A-2033 (2008).
17. Lin, A., Ren, Z., Jia, D. & Wu, X. Co-seismic thrusting slip and shortening structures produced by the 2008 M_w 7.9 Wenchuan earthquake, China. *Eos* **89,** Fall Meet. Suppl., abstr. U23B-0055 (2008).
18. http://news.xinhuanet.com/mil/2008-05/13/content_8161323.htm.
19. http://www.nowpublic.com/world/beichuan-ruins-become-museum-and-memorial.
20. http://neic.usgs.gov/neis/eq_depot/2008/eq_080512_ryan/neic_ryan_cmt.html.
21. Chen, J.-H. *et al.* Seismotectonic study by relocation of the Wenchuan *M*s 8.0 earthquake sequence (in Chinese). *Chin. J. Geophys.* **52,** 390–397 (2009).
22. Hubbard, J. & Shaw, J. H. Uplist of the Longmen Shan and Tibetan plateau, and the 2008 Wenchuan ($M = 7.9$) earthquake. *Nature* **458,** 194–197 (2009).
23. Zhang, P. Z. *et al.* Tectonic model of the great Wenchuan earthquake of May 12, 2008, Sichuan, China. *Chin. Sci. Bull. (Chinese version)* **54,** 944–953 (2009).
24. Shen, Z.-K. *et al.* Postseismic deformation monitoring of the 2008 M_w 7.9 Wenchuan earthquake using GPS. *Eos* **89,** Fall Meet. Suppl., abstr. G33C-0710 (2008).
25. Wang, W.-M., Zhao, L.-F., Li, J. & Yao, Z.-X. Rupture process of the *M*s 8.0 Wenchuan earthquake of Sichuan, China. *Chin. J. Geophys.* **51,** 1403–1410 (2008).
26. Zhang, Y., Feng, W., Xu, L., Zhou, C. & Chen, Y. Spatio-temporal rupture process of the 2008 great Wenchuan earthquake. *Sci. China Ser. D* **52,** 145–154 (2008).
27. Hao, K. X., Si, H., Fujiwara, H. & Ozawa, T. Coseismic surface-rupture and crustal deformations of the 2008 Wenchuan earthquake M_w 7.9, China. *Geophys. Res. Lett.* **36,** L11303 (2009).
28. Deng, Q.-D. (ed.) *Active Tectonics Map of China (in Chinese)* (Seismological Press, 2007).
29. Working Group of the Crustal Motion Observation Network of China Project. Coseismic displacement field of the 2008 *M*s 8.0 Wenchuan earthquake determined by GPS (in Chinese). *Sci. China Ser. D* **38,** 1195–1206 (2008).
30. King, R. W. & Bock, Y. Documentation for the GAMIT GPS analysis software, release 10.0, Mass. Inst. Technol., Cambridge (2000).
31. Dong, D. <http://gipsy.jpl.nasa.gov/qoca>.
32. Wang, M. *et al.* Contemporary crustal deformation of the Chinese continent and tectonic block model. *Sci. China Ser. D Suppl.* **46,** 25–40 (2003).
33. Niu, Z. *et al.* Contemporary velocity field of crustal movement of Chinese mainland from Global Positioning System measurements. *Chin. Sci. Bull* **50,** 939–941 (2005).
34. Gan, W. *et al.* Present-day crustal motion within the Tibetan Plateau inferred from GPS measurements. *J. Geophys. Res.* **112,** B08416 (2007).

Acknowledgements

We thank JAXA and ESA (ESA-NRSCC Dragon project 2577), particularly M. Kawai and R. Malosti for SAR data provision, and CEA and CBSM survey crews, particularly Q. Wang, for GPS data collection. Discussions with X. Xu, C. Lasserre, R. Briggs, X. Wen, Q. Liu, C. Ji, E. Fielding, P. Bird, Y. Kagan, D. Jackson, A. Sladen, J.-P. Avouac, A. Yin and P. Molnar have been helpful. Review comments of J. Langbein are appreciated. Administrative and technical support provided by Q. Li, J. Sun, W. Tao, F. Liang, X. Gao, Y. Wang, M. Hao, K. Wang and W. Chen are appreciated. This study has been supported by research grants from MSTC (2004CB418403, LED2008A05), NSFC (40674011, 40674022), CEA (IGCEA JB-09-04, 200708002) and NSF (EAR-0609656).

Author contributions

Z.-K.S., R.B., Y.Z., P.Z., and J.S. wrote the paper. J.S. and M.W. processed InSAR and GPS data. Y.W. and Z.-K.S. carried out modelling and inversion. P.Z., W.G., H.L., and Q.W. organized GPS field surveys for data collection.

Additional information

Supplementary information accompanies this paper on www.nature.com/naturegeoscience. Reprints and permissions information is available online at http://npg.nature.com/reprintsandpermissions. Correspondence and requests for materials should be addressed to Z.-K.S.

DOI: 10.1038/NGEO636

Note 1. Alternative fault model

In a preliminary model we allowed for only a constant-dip BCF fault plane along the southeast segment. The inversion result yielded a fault with a much shallower (<20°) dip angle and significant slip on a fault stretching more than 45 km down dip. This model does not seem to be realistic physically, and data fitting was much worse than the current model (rejected by F-test at high confidence level).

We still lack a complete structural model from independent data to provide a more detailed 3D fault rupture geometry. However, we hope that more detailed structural models using data and approaches as described for a single cross-section by Hubbard and Shaw[22] will ultimately allow for a more accurate characterization of the geometry.

Note 2. Postseismic deformation and its effect on coseismic displacement estimation

The post-earthquake GPS and SAR data used in this study were measured 1-4 and 1-7 weeks after the quake respectively (postseismic InSAR and GPS epochs are listed in Supplementary Tables 1 and 3, respectively), and postseismic deformation occurred prior to the GPS or InSAR measurements are included in our coseismic displacement estimates. Here we use regional continuous GPS measurements to assess possible effects of postseismic displacements on the estimates of coseismic displacements[24]. Fig. S1 shows the coseismic and postseismic displacement vectors, and data time series of three sites located in the vicinity of the fault rupture. Station PIXI is located about 25 km away from the maximum rupture on the BCF, and has continuous data recording through the year of 2008, with only a few hours of data missing right after the earthquake (due to power failure). The detrended position time series of the site for a 9-month time period spanning the quake, shows a large coseismic offset (~0.7 m), but merely 0-6 mm of poseismic displacements within 5 months after the event (lower left panel, Fig. S1). Following the quake more continuous GPS stations were installed in the vicinity of the fault rupture, whose data help further quantify the temporal behavior of the postseismic deformation[24]. The postseismic displacement time series of a GPS site is modeled using a logarithmic function: $D(t) = D_0 \,\mathrm{Log}(1+t/T)$, where D_0 is the amplitude of the postseismic displacement vector, and T is the logarithmic relaxation time. Using the first six months of data we have estimated a common relaxation time of 8 days (between 4 and 15 days at 95% confidence level) for all the sites[24]. Fig. S1 of lower right panel shows the station position time series of two sites H035 and NR09. The horizontal postseismic displacement amplitudes (D_0) for H035 and NR09 are 9.0 mm and 19.1 mm, respectively. The H035 postseismic displacements accumulated 3 and 7 weeks after the quake would therefore be about 12 mm and 18 mm, respectively (0.49% and 0.74% of the coseismic displacement amplitude). The same estimates for NR09 are 25 mm and 38 mm, respectively (3.0% and 4.5% of the coseismic displacement amplitude). These estimates are obtained on condition that a logarithmic relaxation function is adequate to describe the temporal behavior of postseismic deformation. Substantial evidence supports this model, including continuous GPS time series recorded during the entire postseismic period at permanent sites located more distant from the coseismic rupture of the Wenchuan quake than the two sites mentioned above[24]. Fig. S1 also reveals both coseismic and postseismic displacement vectors at more sites, such as H010, H032, SD07, CHDU, MYAN, and RENS, etc.,

DOI: 10.1038/NGEO636

whose coseismic/postseismic amplude ratios are similar to that of H035 and NR09. Based on the preliminary analysis of the postseismic data we conclude that the early postseismic deformation field should be at least an order of magnitude less than the coseismic slip, and therefore does not significantly affect our estimate of fault slip distribution.

Note 3. Regional tectonics

The Longmen Shan fault system overprinted a Mesozoic orogenic belt during the Late Cenozoic[2,4] as the result of the Indo-Asia collision, when the Tibetan plateau was extruded eastward[S1,S2], thrusting crustal material of the Songpan-Ganzi block onto a deeply rooted and mechanically strong Sichuan basin. Previous geologic studies have found ample evidence of active reverse and dextral faulting for the central sections of the BCF and PGF, but little such evidence has been found for the northeast sections of the faults north of Beichuan[2,8,9]. Pre-earthquake geodetic studies suggest that deformation in the region between the Longmen Shan and Xianshuihe faults is partitioned. The Longriba fault located ~150 km northwest of and parallel to the Longmen Shan fault (Fig. 1) has ~4-6 mm/yr dextral motion, but such a shearing motion diminishes northeastward toward the eastern end of the East Kunlun fault[12,13,S2]. The sinistral motion on the East Kunlun fault, on the other hand, tapers down to < 2 mm/yr toward its eastern end[S2], suggesting that most of the relative motion between the eastern Tibetan plateau and Sichuan basin is accommodated along the East Kunlun and Longriba faults. The remaining part has to be absorbed by tectonic structures located between the two domains. Our derived convergence rate across the central Longmen Shan fault (1.4±0.6 mm/yr) is consistent with Burchfiel et al.'s[2] estimate of 1±1 mm/yr, derived using an earlier version of the GPS dataset than we use here. Our estimates of 1.4±0.6 mm/yr convergence and 1.7±0.6 mm/yr dextral slip across the central Longmen Shan fault system, at the lower bound, also agree with geological estimates of 0.5-0.8 mm/yr convergence and ~1.2 mm/yr dextral slip across both the central BCF and PGF[10]. Considering that other faults such as the WMF located west of the BCF and miscellaneous thrust faults located along the northwestern rim of the Sichuan Basin (e.g. the Longquan and Xiongpo faults[6]) may also make minor contributions to the transpressional motion across the region, the GPS derived regional deformation rates of the past decade are quite consistent with the geological fault slip rates. The lower slip rates of our estimate across the northeastern part of the Longmen Shan (0.8±0.6 mm/yr dextral and 0.3±0.6 mm/yr shortening) are consistent with geological result showing no significant Holocene faulting activities across the faults in the region[8]. Our result is also supported by seismological and tectonic studies on the Minjiang-Huya fault system showing active reverse faulting[S5,S6]. These results explain the mechanism change of coseismic slip, from predominantly thrust at the southwest end to pure dextral at the northeast end of the rupture.

Note 4. GPS and InSAR data processing

Most of the GPS stations had years of preseismic occupation history with the latest survey made less than a year prior to the quake, thus secular deformation before the quake could be readily estimated and separated from the coseismic displacements. The postseismic surveys were conducted 1-7 weeks after the quake. Components of immediate postseismic motions in the coseismic displacement estimates are minor, only a few percent for most of the near and intermediate sites, based on our assessment of postseismic deformation recorded by continuous

GPS sites in the region[24] (see the Supplementary Note 2 for details). 158 horizontal and 46 vertical data points are used (see refs. [29] and [12] for details about the data and processing procedure, and Supplementary Table 3 for data). The selected sites are within 300 km distance from the rupture.

The SAR data are processed using the ROI_PAC software developed at Caltech/JPL (Rosen et. al, 2004), with an ALOS extension coded by Sandwell et al.[S7] The 3-arc-second SRTM data[S8] are interpolated to a 1-arc-second grid for topography phase removal. To process the ALOS and Envisat data we first compute the interferograms and remove the topographic signal. We then geocode the wrapped phase into a geographic coordinate system, and apply a multi-look operation (6-look or 2-look for ALOS or ASAR data respectively to produce ~170 m ground pixel size) before phase unwrapping. This procedure boosts the signal-to-noise ratio of InSAR observations, makes the fringes of the interferograms clearer, and makes phase unwrapping more reliable, especially on the hanging wall side. In the next step we use the minimum cost flow algorithm (MCF) unwrapping module in the Gamma software to unwrap each of the interferograms, which minimizes the phase jumping errors and simultaneously maximizes the availability of InSAR phases[S9]. The unwrapped phase is continuous except at places across the fault rupture. After phase unwrapping, we correct for satellite orbit errors and topography correlated atmospheric effects. This is done by estimating a linear orbit ramp and the DEM-related phase[S10] on the DEM-flattened interferograms using the least squares method, which minimizes the range changes in the far field where no significant deformation is expected. We then remove the DEM-related phase from the data. We find that only path 472 of the ALOS data was disturbed significantly by the effect of atmospheric vertical stratification (DEM-related).

We do not remove the orbit ramp from the data at this stage because its estimate based on the assumption of minimal far field deformation may not be reliable. The far field signals for the ALOS L-band data could be seriously contaminated by ionosphere disturbances, which, according to Sandwell et al.[S7], might be ~16.5 times as large as for the C-band data according to their fequency difference. It is better to do the orbit-ramp correction using GPS data than just assuming flat signals in the far field becuase the unclear far field signal may be far from zero as we expect. The distributed locations of the GPS observation points throughout the interferograms also makes the calibrations more robust. For each path or track we assume a linear orbit ramp, and minimize in a least squares sense the differences between the GPS derived coseismic displacements in the SAR viewing directions and the corresponding quad-tree resampled InSAR points[S11].

After removing the orbit ramp the postfit residuals are less than 3 cm for most of the ALOS PALSAR data and less than 2 cm for most of the Envisat ASAR data. The phase data of paths 472~474 are decorrelated across the fault breaks, and their north and south panels are unwrapped separately. The phase jumps across the fault surface breaks for these three interferograms are also estimated and corrected in the GPS calibration. The constant phase shifts of all the paths and the phase jumps across the fault breaks of paths 472-474 are estimated further in the joint GPS and InSAR dislocation inversion later on. As expected, all of these constant shifts are smaller than 3 cm except for the one of the south part of path 472, which is up to 13.6 cm**.** This is likely because only one GPS data point was available for making the orbit ramp correction of this data panel, and the result might be subject to large errors. We also

DOI: 10.1038/NGEO636

identify regions showing strong long-wavelength, non-earthquake deformation signals, such as the southern parts of paths 471 and 472 and the northern part of path 473. Such problematic data are excluded from the model inversion (Fig. S2).

We apply a quad-tree decomposition algorithm to decimate the InSAR data[S11]. We first expand the InSAR LOS images by padding zeros to empty areas, making the image dimensions to be a power of 2. We then split the expanded image up to four equal quadrants and compute the variance of each quadrant. If the variance of a quadrant is larger than a presumed threshold, the quadrant will be split up to four smaller quadrants. If the variance of a quadrant is lower than the threshold, we compute the mean LOS phase value of the quadrant as its representative deformation measurement. The sub-sampling procedure is done iteratively until convergence. The threshold is set according to the noise level of the InSAR data. It is above the correlation noise level, but low enough so that the deformation gradients are kept as complete as possible. Considering the long strip of ALOS data, we choose three different thresholds for different regions of the data: 2 cm, 2-3 cm, and >3 cm for the near, intermediate, and far fields, respectively. For the ASAR data, the threshold is set to be 1 cm, consistent with its very low noise level.

In the sub-sampling process, we also compute the LOS unit vector of every InSAR point so that the influence of varying view angles can be minimized, especially in the common parts of neighboring tracks/paths.

<u>Note 5. Reweighting of GPS and InSAR data</u>

We have reweighted the GPS and InSAR data as follow. We down-weight the GPS data by adding a factor of $D^{1/4}$ to their original uncertainties, where D is the displacement amplitude in millimeter. Such a treatment is based on the consideration that the near-field GPS data are sensitive to abrupt spatial variations of fault slip and may not be compatible with the smoothing constraint imposed on the fault slip model.

We adopt a conservative strategy dealing with data errors, not accounting for correlation of the InSAR and GPS data in our inversion. This simple approach is widely used in InSAR studies. There have also been studies considering the correlated errors in modeling[S12,S13], but the approaches have not been independently verified, especially using independent observations. Our group developed a 2D full covariance error model to describe the atmospheric delay of radar signals, applied that to the 2008 Nima, Tibet earthquake, and found that it did not have much an impact to our solution[S14]. Furthermore, the current studies on InSAR error correlation have been with C-Band data only, which do not have the kind of long-wavelength disturbance like the ALOS data do. And, the construction of variance/covariance matrix requires that the far field InSAR data be of second order stationary with a zero mean, a condition which could not be met here because of the long-wavelength disturbance in the ALOS data. We therefore choose to use a diagonal error matrix for both the InSAR and GPS data. The uncertainties of the ALOS and ASAR data are set to be 50 mm and 20 mm respectively. Both uncertainties are assigned higher than their nominal uncertainties by a factor of about two, to compensate for neglecting the spatial correlations of the InSAR data errors in data error propagation.

It is still subject to discussion how much weighting relative to GPS data the InSAR data should be assigned. We attempt a range of the InSAR down-weighting factors from 1.5 to 3.0 in test runs. The results do show some changes in solution, such as slight reduction of the largest slip when the GPS data are weighted relatively less; but the first order features, such as the locations and sizes of the peaks and lows, remain unchanged.

Note 6. Identification of fault surface breaks and geometry

We use the amplitude offset data of SAR pairs to locate fault surface breaks, the approach is similar to the one used by Peltzer et al.[S10] The offset-tracking technique of the Gamma software with 64 x 64 windows and 8 x 16 steps on the Single Look Complex data is applied to retrieve the range and azimuth offset fields (Figs. S3 a & b). The results of the offset-tracking processing provide strong constraints on the fault locations of the Wenchuan earthquake. Both the azimuth and range offset data sets are used for fault identification. The former is important for the PGF trace identification, and the latter is good for the BCF rupture identification (Fig. S3). Because the datasets themselves still have multiple wavelength features after removing orbital tilts from the offset field, especially in the azimuth offset data, we do not use these data for modeling. We suspect that the multiple wavelength features were caused by ionosphere disturbance, but further investigation is needed to test this hypothesis.

Concentration of aftershock locations helps identify the surface projections of the faults at the northeast and southwest ends, where the rupture may not have broken to the surface. The surface traces are further smoothed to shape the top boundaries of our fault rupture model. The fault dip angle is assumed constant down-dip, but varies linearly along strike for the entire fault except at Nanba (~104.8°E, 32.2°N). Aftershock locations suggest a right-stepping offset at depth across this location, with a northwest dipping fault plane to the southwest of the fault step and a near vertical geometry to the northeast[21]. We therefore allow a dip angle change across this step-over, separating the fault plane of the BCF into two segments. A uniform dip angle is assumed for the PGF section of the fault plane and treated as unknown in the inversion. Six dip angles at fault nodal points are inverted for in the solution, the other dip angles are either interpolated or tied to the neighbor (for the southwestern end point, Fig. 3a).

Note 7. Meshing and smoothing of fault model

All the fault sections are meshed with small rectangular tiles of ~4×4 km in size. The BCF section of the fault plane is assumed to have 7 rows of patches with 28 km in total width (Fig. 3). A flat fault segment is assumed to branch out from the downdip end of the southwest segment of the BCF (Fig. 3a), and is composed of 7×13 patches. Inclusion of the segment is required by the data (see Note 1). The PGF section of the fault plane is assumed to have 5 rows of patches, and spans 20 km in total down-dip width. Smoothing constraints are imposed for all the neighboring patches, on both the along-strike and down-dip components, with a finite uncertainty of 100 mm assumed for the smoothing conditions. The only exception is at Nanba between the first and second fault segments of the BCF counting from the northeast, where no smoothing is imposed on the neighboring slip components and an abrupt change of the fault dip angle is allowed (Fig. 3). The uncertainty value is chosen by balancing a trade-off curve between the postfit residual χ^2 and the number of parameters resolved in the solution (see ref. [S16] for details of the procedure).

Note 8. Uncertainties in earthquake recurrence interval estimations

The earthquake recurrence intervals across fault segments are derived from estimates of

 DOI: 10.1038/NGEO636

mean fault slip of a characteristic event and interseismic fault slip (or deficit) rates. These estimates are subject to multiple sources of errors, which need to be accounted for to better understand the reliability of these estimates. For derivations of the mean coseismic fault slip across fault segments, we take a mean slip of the top five rows, equivalent to 20 km of fault width. If the downdip width of 20 km does not match the bottom of the seismogenic layer, the mean coseismic slip estimate can be off. We run a test calculating the mean fault slip rates of the top four, five, and six rows of the fault patches (equivalent to 16 km, 20 km, and 24 km of fault width). Our result shows that among the 14 fault segments calculated, 11 have variations of their fault slip estimates of less than 10%, and 3 have variations greater than 10% but less than 20%, respectively. Errors on the fault dip angle estimates have no direct effect on our mean slip estimate, since we assume a listric fault whose balance between the interseismic moment accumulation (proportional to interseismic slip rate) and coseismic moment release (proportional to mean fault slip) does not depend on the dip angle. Variation of degree of smoothing of fault slip would change the mean fault slip estimate a bit, but only by a few percent when the a priori smoothing uncertainty changes between 70 mm and 200 mm.

Estimations on the interseismic fault slip rates, however, suffer from greater uncertainties. The secular shortening rate is 1.4±0.6 mm/yr for the southwest segment and the secular dextral slip rate is 0.8±0.6 mm/yr for the northeast segment of the Longmen Shan fault, respectively, making the errors corresponded to ~43% and ~75% of the signals. The geological estimate of the fault slip rate on the BCF is 0.3-0.6 mm/yr; that is, the error corresponds to ~33% of the signal. Another relatively large error source is the uncertainty of the characteristic events for the fault segments: whether they are independent or joint ruptures on the BCF and PGF. Weighing all these factors, we take only two error sources into consideration in our estimates of earthquake recurrence intervals: uncertainties of the fault slip rates and the characteristic rupture events, since all the other errors are of higher order and would not have much impacts on our final estimates of the recurrence intervals.

Method 1. Fault slip model and Newtonian nonlinear inversion

The slips on individual fault patches are linked to the GPS and InSAR measurements on the Earth's surface using the Okada dislocation code[S17] that allows for the calculation of displacements in a uniform elastic half-space, and the partial derivatives for the nonlinear parameters of six dip angles are derived numerically. We start the model assuming a uniform dip of 50° to the northwest for all the BCF and PGF segments; after about 30 iteration steps the solution converges.

We have 362 GPS and 9110 InSAR data entries in the inversion. The total number of linear model parameters is 1364, which includes 12 InSAR offset terms (1 or 2 terms for each scene depending on whether range-change continuity is preserved across the fault) in addition to the slip components on 676 fault patches. There are another six nonlinear parameters for the dip angles, which are inverted for together with the linear parameters.

We use a Newtonian nonlinear inversion procedure to solve for the coseismic slip distribution, constrained using the GPS and InSAR data. The procedure is as follows.

Let the problem be:

$$\mathbf{y} = \mathbf{A}\mathbf{x} + \mathbf{e},$$

where $\mathbf{y}$ is an $n\times1$ array composed of the GPS and InSAR data, n is the total number of data points. The GPS data are the east, north, and up components of coseismic displacements, and the InSAR data are the coseismic line of sight changes. $\mathbf{x}$ is an array of $m_l\times1$, composed of two parts; the first part involves the along strike and up-dip components of coseismic slip on fault patches, and the second part has the constants of SAR satellite orbit ramp and the across-fault jumps for paths 472, 473, and 474. $\mathbf{A}$ is an $n\times m_l$ array, linking the unknowns of fault slip and the interferogram constants linearly to the observations. $\mathbf{A} = \mathbf{A}(\underline{z})$, $\mathbf{z} = (z_1, z_2, \Lambda\ , z_{m_n})$ are the nonlinear parameters of fault dip angles. $m_n = 6$ for our model. $\mathbf{e}$ is an $n\times1$ array for data errors. $\mathbf{e} = \mathrm{N}(0, \mathrm{C_d})$, $\mathrm{C_d}$ is the variance/covariance matrix of the errors.

We impose a first-order smoothing constraint to the fault slip components, in the form of

$$\mathbf{0} = \mathbf{Gx} + \mathbf{h},$$

where $\mathbf{G}$ is a $p\times m_l$ array for imposing p constraints to the solution. For each pair of adjacent fault tiles (in both along strike and up-dip directions), the entries are 1 and -1 for the corresponding pair of slip components, and 0 for the rest of the components. $\mathbf{h}$ is a $p\times1$ array of a priori errors. $\mathbf{h} = \mathrm{N}(0, \mathrm{C_a})$, $\mathrm{C_a}$ is the variance/covariance matrix of the a priori errors, composed of non-zero diagonal terms only.

The joint equations for data and a priori constraints are:

$$\begin{bmatrix}\mathbf{y}\\ \mathbf{0}\end{bmatrix} = \begin{bmatrix}\mathbf{A}\\ \mathbf{G}\end{bmatrix}\mathbf{x} + \begin{bmatrix}\mathbf{e}\\ \mathbf{h}\end{bmatrix}$$

In the first step we assume a set of nonlinear parameters $\underline{\mathbf{z}}_0$, then $\mathbf{y} = \mathbf{A}(z_0)\mathbf{x} + \mathbf{e}$, a least squares solution yields: $\mathbf{x_0} = \left(\mathbf{A^T C_d^{-1} A} + \mathbf{G^T C_a^{-1} G}\right)^{-1} \mathbf{A^T C_d^{-1} y}$

The first round postfit residuals are:

$$\begin{bmatrix}\mathbf{dy_1}\\ \mathbf{db_1}\end{bmatrix} = \begin{bmatrix}\mathbf{y}\\ \mathbf{0}\end{bmatrix} - \begin{bmatrix}\mathbf{A(z_0)}\\ \mathbf{G}\end{bmatrix}\mathbf{x}_0$$

Taking the first order perturbation of the observables:

$$\mathbf{dy} = \mathbf{Adx} + \frac{\mathbf{dA}}{\mathbf{dz}}\mathbf{xdz} + \mathbf{e}$$

Or: $\mathbf{dy} = [\mathbf{A} \quad \mathbf{B}]\begin{bmatrix}\mathbf{dx}\\ \mathbf{dz}\end{bmatrix}$, where $\mathbf{B} = \frac{\mathbf{dA}}{\mathbf{dz}}\mathbf{x}$, which are the numerically derived partial derivatives with respect to the fault dip angles.

Let the postfit residuals link with parameter increments:

$$\begin{bmatrix}\mathbf{dy_1}\\ \mathbf{db_1}\end{bmatrix} = \begin{bmatrix}\mathbf{A(z_0)} & \mathbf{B(z_0, x_0)}\\ \mathbf{G} & \mathbf{0}\end{bmatrix}\begin{bmatrix}\mathbf{dx}\\ \mathbf{dz}\end{bmatrix} + \begin{bmatrix}\mathbf{e}\\ \mathbf{h}\end{bmatrix}$$

Solve above equations by least squares to obtain $\mathbf{dx}_1$ and $\mathbf{dz}_1$:

$$\begin{bmatrix}\mathbf{dx_1}\\ \mathbf{dz_1}\end{bmatrix} = \left[(\mathbf{A} \quad \mathbf{B})^{\mathbf{T}}\mathbf{C_d^{-1}}(\mathbf{A} \quad \mathbf{B}) + \mathbf{G^T C_a^{-1} G}\right]^{-1}(\mathbf{A} \quad \mathbf{B})^{\mathbf{T}}\mathbf{C_d^{-1}}\begin{pmatrix}\mathbf{dy_1}\\ \mathbf{db_1}\end{pmatrix}$$

 DOI: 10.1038/NGEO636

Let $\mathbf{z}_1 = \mathbf{z}_0 + \mathbf{dz}_1$, $\mathbf{x}_1 = \mathbf{x}_0 + \mathbf{dx}_1$, the second round postfit residuals are:

$$\begin{bmatrix} \mathbf{dy}_2 \\ \mathbf{db}_2 \end{bmatrix} = \begin{bmatrix} \mathbf{y} \\ \mathbf{0} \end{bmatrix} - \begin{bmatrix} \mathbf{A}(\mathbf{z}_1) \\ \mathbf{G} \end{bmatrix} \mathbf{x}_1$$

Then we solve

$$\begin{bmatrix} \mathbf{dy}_2 \\ \mathbf{db}_2 \end{bmatrix} = \begin{bmatrix} \mathbf{A}(\mathbf{z}_1) & \mathbf{B}(\mathbf{z}_1) \\ \mathbf{G} & \mathbf{0} \end{bmatrix} \begin{bmatrix} \mathbf{dx}_2 \\ \mathbf{dz}_2 \end{bmatrix} + \begin{bmatrix} \mathbf{e} \\ \mathbf{h} \end{bmatrix}$$

by least squares to obtain $\mathbf{dx}_2$ and $\mathbf{dz}_2$.

Continue the iteration until the weighted postfit χ^2 reduction becomes trivial. The postfit χ^2 is defined as:

$$\chi^2 = \mathbf{dy}^{\mathbf{T}}\mathbf{C}_{\mathbf{d}}^{-1}\mathbf{dy} + \mathbf{db}^{\mathbf{T}}\mathbf{C}_{\mathbf{d}}^{-1}\mathbf{db}$$

The resolution matrix is[S18]:

$$R = \left(\mathbf{A}^{\mathbf{T}}\mathbf{C}_{\mathbf{d}}^{-1}\mathbf{A} + \mathbf{G}^{\mathbf{T}}\mathbf{C}_{\mathbf{a}}^{-1}\mathbf{G}\right)^{-1}\mathbf{A}^{\mathbf{T}}\mathbf{C}_{\mathbf{d}}^{-1}\mathbf{A}$$

The sum of the diagonal terms of R is the total number of resolution (i.e. the rank of the resolution matrix) resolved by the data. The reduced postfit χ_d^2 due to data is defined as

$$\chi_d^2 = \frac{\mathbf{dy}^{\mathbf{T}}\mathbf{C}_{\mathbf{d}}^{-1}\mathbf{dy}}{n - m_l - m_n}.$$

The inverted fault slip model is listed in Supplementary Table 2, and the GPS data fitting result is in Supplementary Table 3. Among all the slip parameters only 53.5 degrees of freedom are resolved by data, the rest are constrained by the a priori smoothing constraints (see ref. [S18] for resolution interpretation of the inversion). It means that slip on individual fault patches may not be well resolved and reliable; however, slip patterns over a panel of several patches have much better resolution and reliability.

The model is able to achieve 94% reduction of the GPS and InSAR data variance after model fitting, and the reduced posteriori residual χ^2 is 3.70. Such a result suggests that although there may be some parts of the data not well explained, the overall fit is quite reasonable.

As shown in Fig. 2, our optimal model successfully explains most of the deformation signals. Nevertheless there are still some notable patterns left in the residual interferograms. We may have explanations for some of them. For example, the negative range change of up to 30 cm in the region northeast of the PGF surface rupture suggests that a longer PGF rupture is needed to model the deformation field. The phase discontinuity on the interferograms across this section of the fault is not clear (Fig. S2). Discontinuous traces of fault fissures were witnessed along this section of the PGF, but measured offsets were small (~10 cm)[3]. The lack of observations, however, does not preclude the possibility that the PGF may have broken underneath the surface, causing deformation in the region. The negative range change south of Beichuan may have been the result of a similar cause, as the interferogram in the region shows a moderate phase gradient equivalent to a few centimeters of range change. Some large residuals in the intermediate and far field range from the fault were probably produced by atmospheric disturbances and cannot be modeled in this study, such as the ones located at the southern parts of the images of tracks 471, 472, and 476, and at the northern part of the image of track 473 (Figs. 2 and S2).

References

1. Molnar, P., and Tapponnier, P. Cenozoic tectonics of Asia: effects of a continental collision. *Science*, **189**, 419-426 (1975).
2. England, P. C., and Houseman, G. A. Finite strain calculations of continental deformation, 2, Comparison with the India-Asia collision zone. *J. Geophys. Res.*, **91**, 3664-3676 (1986).
3. Xu, X., Wen, X., Chen, G., and Yu, G. Discovery of the Longriba fault zone in eastern Bayan Har block, China and its tectonic implication. *Sci. China Ser. D-Earth Sci*., **51**(9), 1209-1223 (2008).
4. Kirby, E., et al. Slip rate gradients along the eastern Kunlun fault. *Tectonics*, **26**, TC2010, doi:10.1029/2006TC002033 (2007).
5. Jones, L.M., et al. Focal mechanisms of the Songpan earthquakes of August 1976 in Sichuan, China. *J. Geophys. Res*., **89**, 7697–7707 (1984).
6. Kirby, E., et al. Neotectonics of the Min Shan, China: Implications for mechanisms driving Quaternary deformation along the eastern margin of the Tibetan Plateau. *Geol. Soc. Amer. Bull.*, **112**, 375-393 (2000).
7. Sandwell, D., et al. Accuracy and resolution of ALOS interferometry: Vector deformation maps of the Father's Day intrusion at Kilauea. *IEEE Transactions on Geoscience and Remote Sensing* (2007).
8. Farr T. G., et al. The shuttle radar topography mission. *Rev. Geophys*., **45**, RG2004, doi:10.1029/2005RG000183 (2007).
9. Wegmuller, U., and Werner, C. Retrieval of vegetation parameters with SAR Interferometry. *IEEE Transactions on Geoscience and Remote Sensing*, **35**(1), 18-24 (1997).
10. Hanssen, R. F. *Radar interferometry: Data interpretation and error analysis*, Kluwer Academic Publishers, Dordrecht (2001).
11. Jónsson, S., et al. Fault slip distribution of the 1999 M-w 7.1 Hector Mine, California, earthquake, estimated from satellite radar and GPS measurements. *Bull. Seismol. Soc. Am.*, **92**(4), 1377-1389 (2002).
12. Sudhaus, H., and S. Jónsson. Improved source modelling through combined use of InSAR and GPS under consideration of correlated data errors: application to the June 2000 Kleifarvatn earthquake, Iceland. *Geophysical Journal International*, **176**(2), 353-655 (2009).
13. Funning, G. J., et al. Surface displacements and source parameters of the 2003 Bam (Iran) earthquake from Envisat advanced synthetic aperture radar imagery. *J. Geophys. Res.*, **110**, B09406, doi:10.1029/2004JB003338 (2005).
14. Sun, J., et al. Synthetic Normal faulting of the 9 January 2008 Nima (Tibet) Earthquake

DOI: 10.1038/NGEO636

from Conventional and Along-track SAR Interferometry. *Geophys. Res. Lett*., **35**, L22308, doi:10.1029/2008GL035691 (2008).

15. Peltzer, G.., et al. Evidence of nonlinear elasticity of the crust from the Mw7.6 Manyi (Tibet) earthquake. *Science*, **286**(5438), 272-276 (1999).
16. Shen, Z.-K., et al. Northridge earthquake rupture models based on the global positioning system measurements. *Bull. Seismol. Soc. Am*., **86**, 1B, S37-S48 (1996).
17. Okada, Y. Internal deformation due to shear and tensile faults in a half-space. *Bull. Seism. Soc. Am.*, **82**, 1018-1040 (1992).
18. Jackson, D. D., and M. A. Matsu'ura. A Bayesian approach to nonlinear inversion. *J. Geophys. Res.*, **90**, 581-591 (1985).

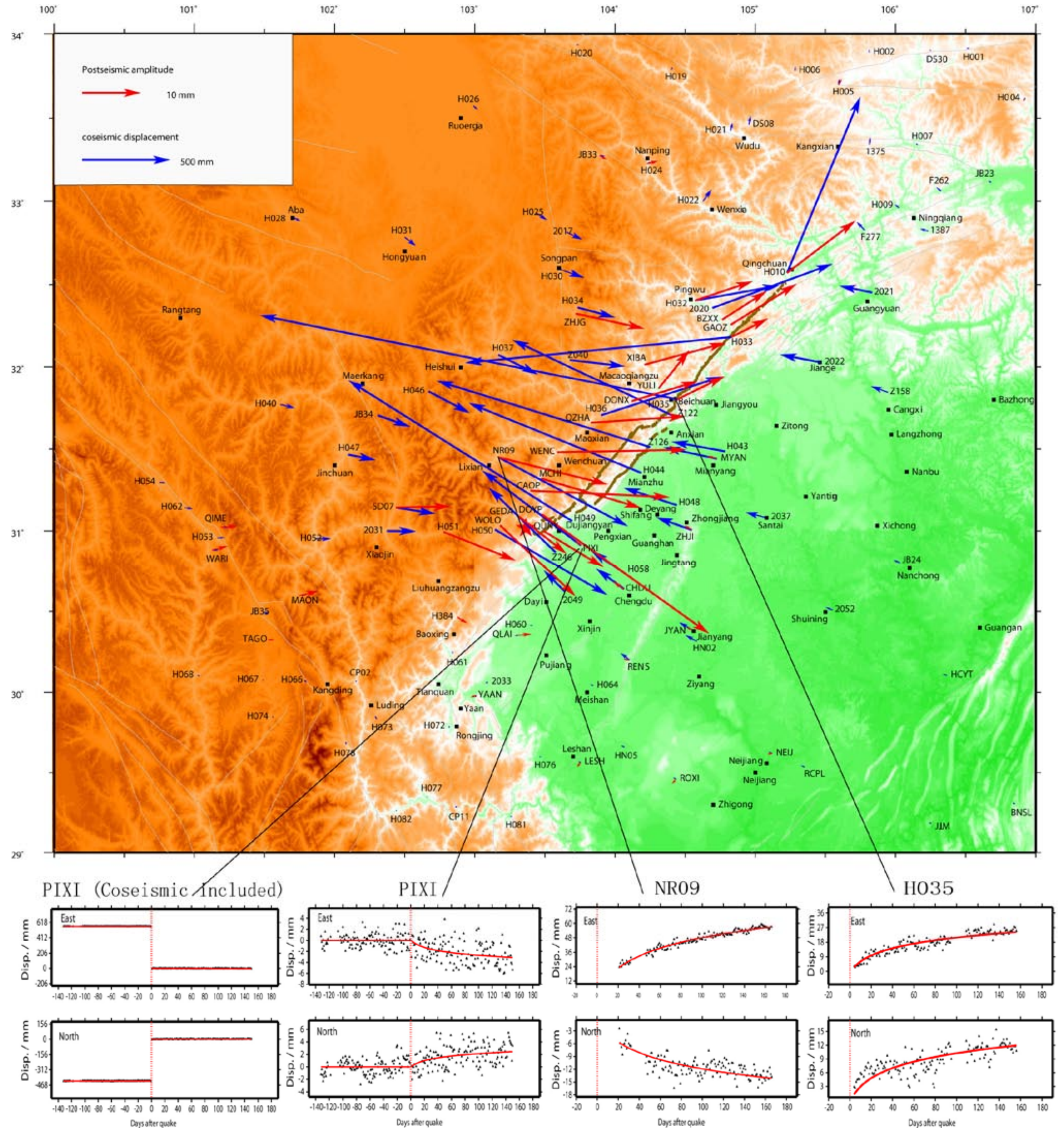

Figure S1. Upper panel: station coseismic (blue arrows) and postseismic (red arrows) displacement vectors (Note the different scale of arrows shown in inset legend). The postseismic displacements are presented as amplitudes of logarithmic functions, equivalent to accumulated displacements at the 14th day after the quake. Lower right panel: horizontal components of postseismic displacement time series for stations H035 and NR09; black triangles are the data, red curves are those predicted by a logarithmic relaxation model with a time constant of 8 days. Red vertical dashed lines mark the epoch of earthquake occurrence. Lower left panel: horizontal components of pre- and post-seismic displacement time series for station PIXI, with and without coseismic displacement jumps.

DOI: 10.1038/NGEO636

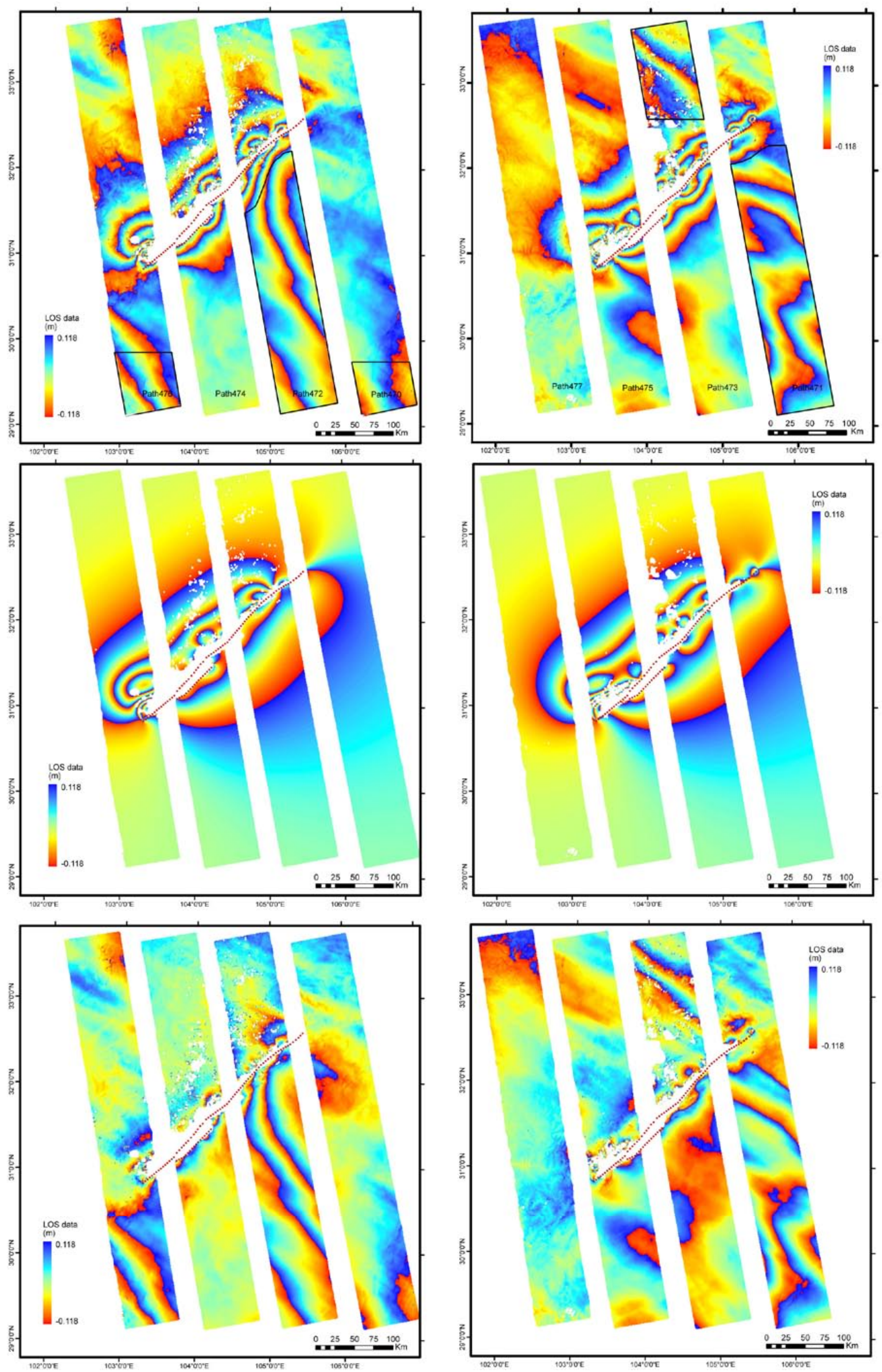

DOI: 10.1038/NGEO636

Figure S2. ALOS InSAR data fitting. The figures are the same as in Fig. 2 except that the interferograms are not shadowed by their neighbors. Top panel: observations (portions of data not used in modeling are delineated with black frames). Left and right panels show even and odd numbered ALOS path interferograms, respectively. Central panel: model predicted, and bottom panel: postfit residuals. Red dots are the surface nodal points of fault model patches.

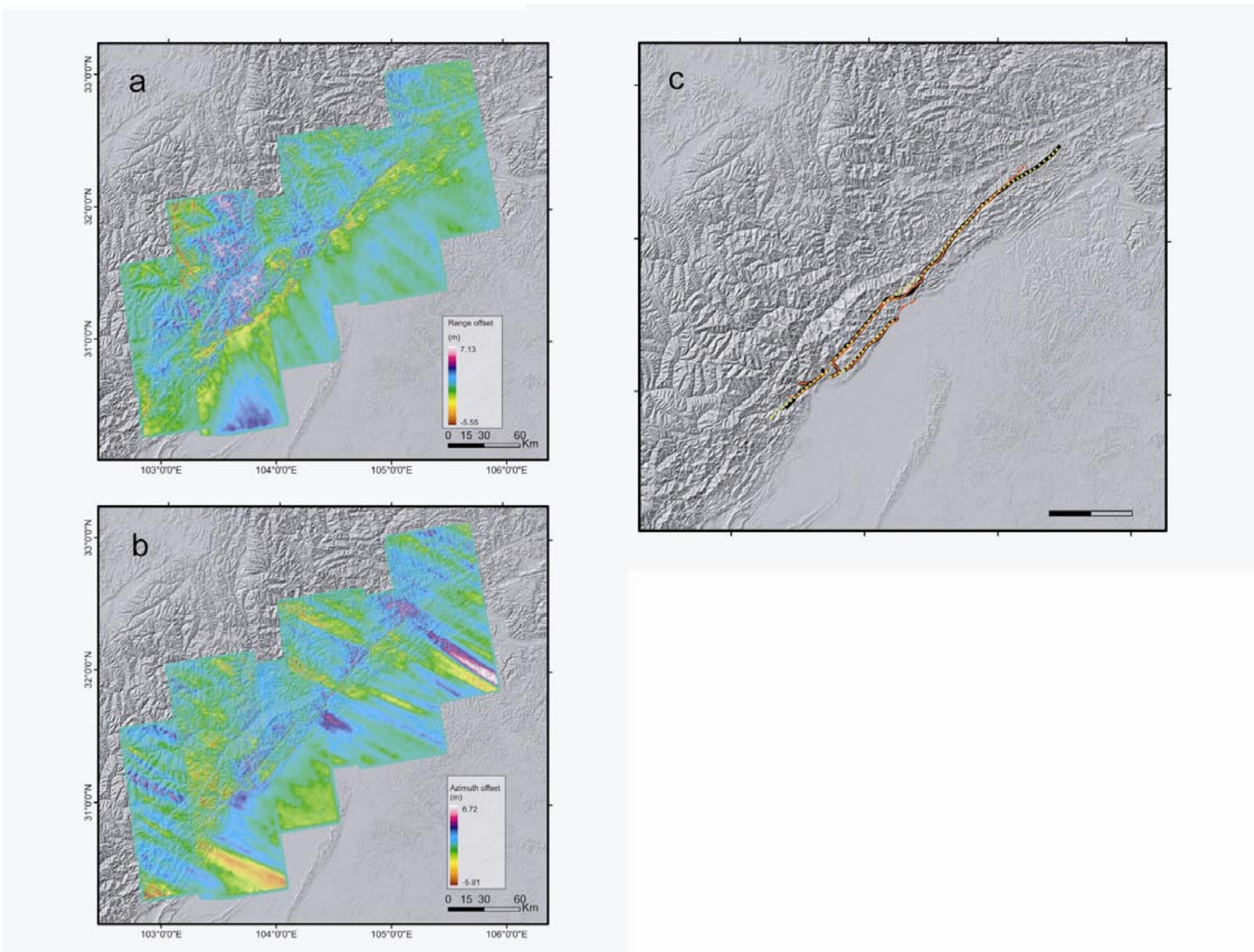

Figure S3. Identification of fault surface breaks. a) ALOS range offsets and traces of identified fault breaks. b) ALOS azimuth offsets and traces of identified fault breaks. c) Comparison of fault surface breaks. Red lines: inferred from the SAR data, black lines: mapped by field geologists[3], and yellow dots: surface nodal points of fault patches used in this study. Our result differs from that of Xu et al.[3] at the northeast end of the rupture. Theirs was based on aftershock locations and may not be as accurate as our reading of the SAR interferograms.

 DOI: 10.1038/NGEO636

Table 1. SAR data used for derivation of coseismic displacements of the Wenchuan earthquake.

Path/Track	Frame	θ^a	Pre-seismic epoch	Post-seismic epoch	$B_{\perp,}{}^{b}(m)$	Orbit direction [c]
ALOS 470	580-650	38.7°	09 Feb 2007	29 Jun 2008	-90	A
ALOS 471	580-650	38.7°	29 Feb 2008	31 May 2008	90	A
ALOS 472	580-650	38.7°	28 Jan 2007	17 Jun 2008	203	A
ALOS 473	580-650	38.7°	17 Feb 2008	19 May 2008	225	A
ALOS 474	580-650	38.7°	05 Mar 2008	05 Jun 2008	283	A
ALOS 475	580-650	38.7°	20 Jun 2007	22 Jun 2008	-34	A
ALOS 476	580-650	38.7°	08 Apr 2008	24 May 2008	-300	A
ALOS 477	580-650	38.7°	25 Apr 2008	10 Jun 2008	-70	A
ASAR 290	2961-3015	22.8°	03 Mar 2008	16 Jun 2008	-474	D

[a] Incidence angle in the swath center

[b] Perpendicular baseline between pre- and post-seismic satellite orbits

[c] A for ascending pass, D for descending pass.

Table 2 Fault slip model.

Index	Length/km	Wid/km	Depth/km	Dip/°	Strike/°	Lat/°N	Long/°E	SS/mm	TS/mm*
1	3.8142	4	3.9730	96.66	-137.01	32.6194	105.4699	-1437.08	1250.42
2	3.8151	4	7.9605	96.66	-135.90	32.6168	105.4732	-1447.38	1181.39
3	3.8189	4	11.9407	96.66	-134.78	32.6140	105.4764	-1463.85	996.27
4	3.8259	4	15.9210	96.66	-133.67	32.6112	105.4795	-1456.66	814.82
5	3.8359	4	19.9012	96.66	-132.56	32.6084	105.4826	-1434.74	681.21
6	3.8489	4	23.8815	96.66	-131.45	32.6055	105.4855	-1411.91	601.32
7	3.8648	4	27.8617	96.66	-130.34	32.6025	105.4884	-1397.95	566.45
8	3.8162	4	3.9875	94.53	-137.00	32.5953	105.4410	-1521.34	1303.18
9	3.8192	4	7.9713	94.53	-134.78	32.5932	105.4434	-1528.88	1210.42
10	3.8267	4	11.9570	94.53	-132.55	32.5912	105.4457	-1517.20	979.33
11	3.8388	4	15.9427	94.53	-130.34	32.5890	105.4479	-1482.56	780.39
12	3.8552	4	19.9283	94.53	-128.14	32.5868	105.4500	-1442.10	649.19
13	3.8761	4	23.9140	94.53	-125.96	32.5846	105.4521	-1410.28	580.40
14	3.9014	4	27.8997	94.53	-123.79	32.5823	105.4541	-1396.00	559.92
15	3.8152	4	3.9965	92.40	-136.99	32.5711	105.4121	-1621.03	1184.26
16	3.8197	4	7.9893	92.40	-134.76	32.5700	105.4133	-1615.12	1102.68
17	3.8241	4	11.9840	92.40	-132.53	32.5689	105.4145	-1568.47	911.65
18	3.8285	4	15.9786	92.40	-130.30	32.5677	105.4157	-1507.56	741.38
19	3.8329	4	19.9733	92.40	-128.08	32.5666	105.4168	-1453.27	630.61
20	3.8372	4	23.9679	92.40	-125.85	32.5653	105.4178	-1417.12	577.04
21	3.8416	4	27.9626	92.40	-123.63	32.5641	105.4188	-1403.83	568.35
22	4.5089	4	4.0000	90.27	-127.80	32.5470	105.3780	-1623.76	1106.49
23	4.5247	4	7.9962	90.27	-125.93	32.5469	105.3782	-1619.42	1013.58
24	4.5399	4	11.9943	90.27	-124.06	32.5468	105.3783	-1571.81	866.95
25	4.5546	4	15.9924	90.27	-122.20	32.5467	105.3785	-1508.60	735.04
26	4.5688	4	19.9906	90.27	-120.34	32.5466	105.3786	-1456.98	646.65
27	4.5823	4	23.9887	90.27	-118.49	32.5465	105.3788	-1427.33	604.08
28	4.5953	4	27.9868	90.27	-116.64	32.5463	105.3789	-1421.87	600.68
29	4.5089	4	3.9979	88.13	-127.80	32.5232	105.3390	-1650.09	1137.31
30	4.5113	4	7.9921	88.13	-125.91	32.5242	105.3382	-1608.17	1036.03
31	4.5137	4	11.9881	88.13	-124.02	32.5251	105.3374	-1546.98	915.86
32	4.5162	4	15.9841	88.13	-122.13	32.5261	105.3367	-1495.57	803.17
33	4.5186	4	19.9802	88.13	-120.25	32.5271	105.3360	-1463.08	718.03
34	4.5211	4	23.9762	88.13	-118.36	32.5282	105.3353	-1450.72	669.68
35	4.5235	4	27.9722	88.13	-116.48	32.5292	105.3347	-1458.15	659.41
36	4.5104	4	3.9903	86.00	-127.78	32.4994	105.3001	-1772.98	1223.97
37	4.4811	4	7.9769	86.00	-125.91	32.5015	105.2984	-1629.38	1200.68
38	4.4498	4	11.9653	86.00	-124.04	32.5037	105.2969	-1538.82	1120.29
39	4.4163	4	15.9537	86.00	-122.15	32.5059	105.2955	-1504.59	989.19
40	4.3806	4	19.9421	86.00	-120.25	32.5081	105.2942	-1496.37	866.62
41	4.3427	4	23.9306	86.00	-118.35	32.5104	105.2930	-1502.36	782.02

DOI: 10.1038/NGEO636

42	4.3026	4	27.9190	86.00	-116.43	32.5127	105.2919	-1521.06	743.72
43	3.5213	4	3.9771	83.87	-119.29	32.4806	105.2643	-1862.52	1411.48
44	3.5038	4	7.9506	83.87	-116.84	32.4840	105.2621	-1687.05	1518.02
45	3.4852	4	11.9259	83.87	-114.38	32.4874	105.2601	-1615.02	1441.01
46	3.4655	4	15.9012	83.87	-111.90	32.4909	105.2583	-1596.55	1250.03
47	3.4450	4	19.8765	83.87	-109.40	32.4945	105.2567	-1596.60	1059.10
48	3.4235	4	23.8518	83.87	-106.89	32.4981	105.2552	-1604.56	917.45
49	3.4014	4	27.8271	83.87	-104.35	32.5018	105.2540	-1619.02	836.34
50	3.5231	4	3.9585	81.74	-119.29	32.4663	105.2308	-1965.96	1711.90
51	3.5260	4	7.9133	81.74	-116.90	32.4709	105.2280	-1843.57	1880.83
52	3.5291	4	11.8700	81.74	-114.51	32.4756	105.2254	-1784.39	1755.08
53	3.5326	4	15.8267	81.74	-112.12	32.4804	105.2231	-1755.52	1486.45
54	3.5365	4	19.7833	81.74	-109.73	32.4852	105.2211	-1739.18	1222.62
55	3.5408	4	23.7400	81.74	-107.35	32.4902	105.2193	-1731.90	1024.12
56	3.5458	4	27.6967	81.74	-104.97	32.4952	105.2177	-1734.72	903.54
57	3.5222	4	3.9344	79.61	-119.28	32.4519	105.1972	-2108.58	1843.69
58	3.5250	4	7.8651	79.61	-116.90	32.4577	105.1938	-2081.71	2048.32
59	3.5280	4	11.7977	79.61	-114.52	32.4636	105.1906	-2035.33	1907.66
60	3.5313	4	15.7302	79.61	-112.15	32.4696	105.1877	-1976.51	1603.57
61	3.5347	4	19.6628	79.61	-109.78	32.4757	105.1851	-1922.27	1301.55
62	3.5384	4	23.5953	79.61	-107.41	32.4819	105.1828	-1883.17	1069.96
63	3.5424	4	27.5279	79.61	-105.04	32.4882	105.1808	-1863.76	924.27
64	3.5241	4	3.9048	77.48	-119.28	32.4376	105.1637	-2272.24	1761.30
65	3.5267	4	7.8060	77.48	-116.92	32.4445	105.1596	-2334.55	1943.93
66	3.5305	4	11.7090	77.48	-114.57	32.4516	105.1557	-2306.09	1820.64
67	3.5359	4	15.6120	77.48	-112.21	32.4588	105.1522	-2216.79	1541.72
68	3.5433	4	19.5150	77.48	-109.87	32.4662	105.1490	-2119.17	1255.36
69	3.5530	4	23.4180	77.48	-107.53	32.4736	105.1462	-2041.41	1028.98
70	3.5654	4	27.3210	77.48	-105.19	32.4811	105.1438	-1994.00	882.13
71	3.5232	4	3.8698	75.34	-119.27	32.4232	105.1302	-2451.60	1510.42
72	3.5901	4	7.7361	75.34	-117.03	32.4312	105.1251	-2558.58	1614.38
73	3.6598	4	11.6042	75.34	-114.84	32.4393	105.1202	-2537.07	1521.08
74	3.7329	4	15.4722	75.34	-112.69	32.4475	105.1158	-2426.36	1308.68
75	3.8094	4	19.3403	75.34	-110.60	32.4559	105.1116	-2294.27	1081.71
76	3.8898	4	23.2083	75.34	-108.54	32.4644	105.1079	-2182.34	896.10
77	3.9744	4	27.0764	75.34	-106.54	32.4730	105.1045	-2108.86	773.04
78	3.9707	4	3.8295	73.21	-125.69	32.4056	105.0948	-2610.33	1188.70
79	4.0663	4	7.6555	73.21	-123.65	32.4142	105.0881	-2706.43	1188.76
80	4.1658	4	11.4832	73.21	-121.66	32.4231	105.0817	-2687.23	1105.67
81	4.2687	4	15.3110	73.21	-119.72	32.4322	105.0757	-2568.16	961.69
82	4.3747	4	19.1387	73.21	-117.83	32.4414	105.0701	-2417.30	811.23
83	4.4834	4	22.9664	73.21	-115.98	32.4507	105.0648	-2283.57	687.90
84	4.5946	4	26.7942	73.21	-114.17	32.4602	105.0599	-2193.19	607.87

85	4.3541	4	3.7839	71.08	-128.94	32.3835	105.0581	-2772.09	905.89
86	4.3886	4	7.5643	71.08	-127.10	32.3929	105.0499	-2823.72	808.31
87	4.4253	4	11.3464	71.08	-125.26	32.4025	105.0421	-2776.96	697.45
88	4.4636	4	15.1285	71.08	-123.45	32.4123	105.0346	-2646.13	594.04
89	4.5031	4	18.9107	71.08	-121.64	32.4223	105.0275	-2486.06	507.93
90	4.5433	4	22.6928	71.08	-119.85	32.4325	105.0208	-2342.13	445.57
91	4.5837	4	26.4749	71.08	-118.08	32.4429	105.0145	-2243.24	412.37
92	4.3534	4	3.7330	68.95	-128.93	32.3599	105.0211	-2908.18	708.37
93	4.3549	4	7.4626	68.95	-127.11	32.3702	105.0119	-2910.07	518.78
94	4.3571	4	11.1939	68.95	-125.29	32.3807	105.0030	-2823.25	374.74
95	4.3600	4	14.9252	68.95	-123.47	32.3915	104.9946	-2675.58	285.04
96	4.3632	4	18.6564	68.95	-121.65	32.4025	104.9866	-2508.14	234.70
97	4.3667	4	22.3877	68.95	-119.83	32.4137	104.9789	-2359.03	213.56
98	4.3703	4	26.1190	68.95	-118.01	32.4251	104.9717	-2256.17	216.16
99	4.3555	4	3.6770	66.82	-128.93	32.3362	104.9841	-2962.66	613.44
100	4.3640	4	7.3506	66.82	-127.14	32.3475	104.9740	-2930.26	365.43
101	4.3707	4	11.0258	66.82	-125.35	32.3590	104.9643	-2818.12	184.67
102	4.3758	4	14.7011	66.82	-123.56	32.3708	104.9550	-2658.37	75.87
103	4.3792	4	18.3764	66.82	-121.78	32.3828	104.9462	-2484.51	26.24
104	4.3809	4	22.0517	66.82	-119.99	32.3951	104.9378	-2332.28	20.08
105	4.3810	4	25.7270	66.82	-118.21	32.4076	104.9299	-2229.00	42.40
106	3.9707	4	3.6159	64.68	-129.39	32.3134	104.9488	-2933.81	683.11
107	3.9787	4	7.2284	64.68	-127.46	32.3257	104.9377	-2880.29	407.10
108	3.9852	4	10.8425	64.68	-125.53	32.3382	104.9272	-2763.30	159.94
109	3.9903	4	14.4567	64.68	-123.60	32.3510	104.9171	-2595.66	-10.86
110	3.9940	4	18.0709	64.68	-121.68	32.3641	104.9075	-2416.60	-97.45
111	3.9966	4	21.6851	64.68	-119.76	32.3774	104.8985	-2263.96	-116.35
112	3.9984	4	25.2993	64.68	-117.83	32.3910	104.8899	-2164.01	-92.67
113	3.9699	4	3.5497	62.55	-129.38	32.2917	104.9152	-2912.40	921.60
114	3.9713	4	7.0962	62.55	-127.48	32.3049	104.9033	-2824.26	620.77
115	3.9789	4	10.6442	62.55	-125.58	32.3183	104.8918	-2675.81	271.78
116	3.9935	4	14.1923	62.55	-123.70	32.3321	104.8809	-2489.81	4.68
117	4.0162	4	17.7404	62.55	-121.82	32.3461	104.8705	-2304.86	-147.43
118	4.0477	4	21.2885	62.55	-119.96	32.3604	104.8606	-2155.59	-199.35
119	4.0889	4	24.8366	62.55	-118.13	32.3750	104.8512	-2064.91	-185.86
120	3.9719	4	3.4787	60.42	-129.38	32.2700	104.8817	-2938.18	1286.47
121	4.1511	4	6.9541	60.42	-127.81	32.2834	104.8681	-2756.17	923.81
122	4.3326	4	10.4312	60.42	-126.30	32.2972	104.8550	-2535.50	481.06
123	4.5176	4	13.9083	60.42	-124.84	32.3113	104.8424	-2327.42	103.27
124	4.7071	4	17.3854	60.42	-123.44	32.3257	104.8302	-2145.70	-134.64
125	4.9024	4	20.8624	60.42	-122.09	32.3403	104.8184	-2011.27	-234.38
126	5.1042	4	24.3395	60.42	-120.78	32.3552	104.8071	-1942.31	-237.54
127	4.4786	4	3.4028	58.29	-139.14	32.2421	104.8462	-2959.37	1796.40

DOI: 10.1038/NGEO636

128	4.6474	4	6.8025	58.29	-137.41	32.2554	104.8304	-2591.42	1314.27
129	4.8315	4	10.2037	58.29	-135.75	32.2690	104.8150	-2307.38	779.31
130	5.0297	4	13.6050	58.29	-134.17	32.2829	104.7999	-2103.57	286.67
131	5.2410	4	17.0062	58.29	-132.67	32.2971	104.7852	-1952.61	-47.54
132	5.4642	4	20.4075	58.29	-131.23	32.3116	104.7709	-1856.13	-208.88
133	5.6985	4	23.8087	58.29	-129.87	32.3263	104.7569	-1825.43	-242.90
134	4.4793	4	3.3222	56.16	-139.13	32.2123	104.8141	-3054.20	2512.95
135	4.4791	4	6.7251	56.16	-138.33	32.2255	104.7966	-2542.51	1794.91
136	4.4960	4	10.0876	56.16	-137.54	32.2389	104.7794	-2212.17	1106.56
137	4.5288	4	13.4501	56.16	-136.75	32.2525	104.7626	-1992.55	523.39
138	4.5760	4	16.8127	56.16	-135.96	32.2664	104.7459	-1853.38	117.10
139	4.6363	4	20.1752	56.16	-135.17	32.2805	104.7296	-1780.64	-109.97
140	4.7085	4	23.5377	56.16	-134.39	32.2949	104.7135	-1764.83	-203.53
141	3.9238	4	3.0607	49.92	-137.41	32.1867	104.7821	-3049.35	3222.78
142	3.9234	4	6.1208	49.92	-137.42	32.2024	104.7620	-2478.67	2629.14
143	3.9229	4	9.1812	49.92	-137.42	32.2180	104.7418	-1880.72	2033.08
144	3.9224	4	12.2416	49.92	-137.42	32.2337	104.7217	-1396.17	1523.29
145	3.9218	4	15.3020	49.92	-137.43	32.2494	104.7015	-1076.98	1146.38
146	3.9212	4	18.3624	49.92	-137.43	32.2650	104.6813	-910.21	906.91
147	3.9205	4	21.4228	49.92	-137.43	32.2807	104.6612	-856.31	781.99
148	3.9252	4	3.0601	49.91	-137.42	32.1607	104.7539	-2814.59	2833.14
149	3.9241	4	6.1203	49.91	-137.42	32.1764	104.7338	-2328.55	2239.10
150	3.9231	4	9.1804	49.91	-137.42	32.1921	104.7136	-1778.24	1749.67
151	3.9219	4	12.2405	49.91	-137.42	32.2077	104.6935	-1339.27	1329.91
152	3.9207	4	15.3006	49.91	-137.42	32.2234	104.6733	-1055.10	1008.87
153	3.9195	4	18.3608	49.91	-137.42	32.2391	104.6531	-914.27	800.60
154	3.9182	4	21.4209	49.91	-137.42	32.2548	104.6330	-887.01	695.29
155	3.9249	4	3.0596	49.90	-137.40	32.1347	104.7257	-2551.20	2567.01
156	3.9238	4	6.1192	49.90	-137.40	32.1504	104.7056	-2110.76	2055.94
157	3.9228	4	9.1788	49.90	-137.40	32.1661	104.6854	-1717.60	1587.66
158	3.9218	4	12.2383	49.90	-137.40	32.1818	104.6653	-1389.62	1186.01
159	3.9207	4	15.2979	49.90	-137.40	32.1975	104.6451	-1153.85	882.51
160	3.9197	4	18.3575	49.90	-137.40	32.2131	104.6249	-1021.01	685.51
161	3.9186	4	21.4171	49.90	-137.41	32.2288	104.6048	-984.48	585.98
162	3.9262	4	3.0590	49.89	-137.40	32.1087	104.6975	-2565.03	2461.75
163	3.9252	4	6.1181	49.89	-137.40	32.1244	104.6774	-2200.99	2026.68
164	3.9248	4	9.1771	49.89	-137.40	32.1401	104.6572	-1870.78	1530.19
165	3.9251	4	12.2362	49.89	-137.40	32.1558	104.6371	-1586.28	1085.93
166	3.9261	4	15.2952	49.89	-137.41	32.1715	104.6169	-1357.57	756.55
167	3.9277	4	18.3543	49.89	-137.41	32.1872	104.5967	-1201.92	550.80
168	3.9298	4	21.4133	49.89	-137.41	32.2028	104.5766	-1130.26	453.88
169	3.9259	4	3.0585	49.87	-137.38	32.0828	104.6693	-2688.90	2414.34
170	3.9995	4	6.1170	49.87	-137.41	32.0982	104.6489	-2410.40	1997.29

171	4.0725	4	9.1755	49.87	-137.44	32.1136	104.6285	-2132.43	1471.69
172	4.1447	4	12.2340	49.87	-137.47	32.1291	104.6081	-1859.29	976.46
173	4.2163	4	15.2925	49.87	-137.50	32.1445	104.5876	-1606.44	609.33
174	4.2873	4	18.3510	49.87	-137.53	32.1599	104.5672	-1406.81	392.21
175	4.3577	4	21.4095	49.87	-137.55	32.1753	104.5468	-1289.03	306.46
176	3.7804	4	3.0580	49.86	-140.70	32.0556	104.6415	-2847.02	2414.24
177	3.8546	4	6.1159	49.86	-140.67	32.0706	104.6206	-2631.92	1987.39
178	3.9281	4	9.1739	49.86	-140.65	32.0855	104.5996	-2391.65	1421.46
179	4.0009	4	12.2318	49.86	-140.62	32.1005	104.5787	-2116.07	864.77
180	4.0730	4	15.2898	49.86	-140.59	32.1154	104.5578	-1828.90	458.93
181	4.1446	4	18.3478	49.86	-140.57	32.1304	104.5369	-1584.58	237.17
182	4.2156	4	21.4057	49.86	-140.55	32.1453	104.5160	-1426.53	171.40
183	3.7817	4	3.0574	49.85	-140.71	32.0293	104.6161	-3027.63	2471.10
184	3.7808	4	6.1148	49.85	-140.71	32.0440	104.5949	-2864.44	2006.49
185	3.7805	4	9.1723	49.85	-140.71	32.0587	104.5737	-2618.97	1378.14
186	3.7809	4	12.2297	49.85	-140.71	32.0734	104.5525	-2301.18	766.00
187	3.7820	4	15.2871	49.85	-140.71	32.0881	104.5313	-1969.53	338.20
188	3.7836	4	18.3445	49.85	-140.72	32.1028	104.5102	-1691.39	125.14
189	3.7858	4	21.4019	49.85	-140.72	32.1175	104.4890	-1512.84	83.40
190	3.7813	4	3.0569	49.84	-140.69	32.0030	104.5907	-3177.68	2575.91
191	3.7801	4	6.1138	49.84	-140.69	32.0177	104.5695	-3039.15	2053.63
192	3.7789	4	9.1706	49.84	-140.69	32.0324	104.5483	-2762.22	1346.86
193	3.7776	4	12.2275	49.84	-140.69	32.0471	104.5271	-2390.11	699.63
194	3.7764	4	15.2844	49.84	-140.69	32.0618	104.5060	-2017.83	273.36
195	3.7752	4	18.3413	49.84	-140.70	32.0765	104.4848	-1721.02	81.09
196	3.7740	4	21.3981	49.84	-140.70	32.0912	104.4636	-1540.99	65.83
197	3.7832	4	3.0563	49.83	-140.68	31.9767	104.5653	-3271.85	2741.27
198	3.7822	4	6.1127	49.83	-140.68	31.9914	104.5441	-3122.77	2156.02
199	3.7813	4	9.1690	49.83	-140.68	32.0061	104.5229	-2792.97	1375.95
200	3.7803	4	12.2253	49.83	-140.68	32.0208	104.5018	-2370.56	714.22
201	3.7793	4	15.2817	49.83	-140.69	32.0355	104.4806	-1976.59	306.98
202	3.7783	4	18.3380	49.83	-140.69	32.0502	104.4594	-1683.76	139.07
203	3.7774	4	21.3943	49.83	-140.69	32.0649	104.4382	-1522.22	143.37
204	3.7822	4	3.0558	49.81	-140.67	31.9504	104.5399	-3302.69	2979.43
205	3.7812	4	6.1116	49.81	-140.67	31.9651	104.5187	-3091.12	2339.36
206	3.7802	4	9.1674	49.81	-140.68	31.9798	104.4975	-2689.69	1513.00
207	3.7793	4	12.2232	49.81	-140.68	31.9945	104.4764	-2239.62	863.65
208	3.7783	4	15.2790	49.81	-140.68	32.0092	104.4552	-1860.60	480.34
209	3.7774	4	18.3347	49.81	-140.68	32.0239	104.4340	-1603.00	324.74
210	3.7764	4	21.3905	49.81	-140.68	32.0386	104.4128	-1480.89	329.36
211	3.7826	4	3.0552	49.80	-140.66	31.9241	104.5145	-3281.39	3286.91
212	3.7819	4	6.1105	49.80	-140.67	31.9388	104.4933	-2915.65	2645.35
213	3.7811	4	9.1657	49.80	-140.67	31.9535	104.4721	-2455.02	1830.95

DOI: 10.1038/NGEO636

214	3.7804	4	12.2210	49.80	-140.67	31.9682	104.4510	-2032.23	1204.81
215	3.7797	4	15.2762	49.80	-140.67	31.9829	104.4298	-1715.08	822.81
216	3.7790	4	18.3315	49.80	-140.67	31.9976	104.4086	-1521.70	645.81
217	3.7782	4	21.3867	49.80	-140.67	32.0124	104.3874	-1452.88	618.10
218	3.7839	4	3.0547	49.79	-140.67	31.8978	104.4891	-3338.99	3672.20
219	3.7829	4	6.1094	49.79	-140.67	31.9125	104.4679	-2803.46	3092.84
220	3.7820	4	9.1641	49.79	-140.67	31.9272	104.4467	-2276.57	2353.19
221	3.7810	4	12.2188	49.79	-140.67	31.9419	104.4256	-1884.45	1737.84
222	3.7800	4	15.2735	49.79	-140.67	31.9566	104.4044	-1634.16	1315.97
223	3.7791	4	18.3282	49.79	-140.67	31.9714	104.3832	-1503.28	1073.61
224	3.7781	4	21.3829	49.79	-140.68	31.9861	104.3621	-1478.89	977.16
225	3.7835	4	3.0542	49.78	-140.65	31.8715	104.4637	-3624.10	4157.16
226	3.7774	4	6.1083	49.78	-140.65	31.8862	104.4425	-2963.34	3602.91
227	3.7713	4	9.1625	49.78	-140.65	31.9009	104.4214	-2344.75	2942.05
228	3.7653	4	12.2166	49.78	-140.65	31.9157	104.4002	-1935.38	2343.43
229	3.7593	4	15.2708	49.78	-140.65	31.9304	104.3791	-1709.68	1864.43
230	3.7537	4	18.3250	49.78	-140.66	31.9452	104.3579	-1601.58	1531.68
231	3.7487	4	21.3791	49.78	-140.66	31.9599	104.3368	-1586.58	1346.33
232	4.1996	4	3.0536	49.77	-140.42	31.8438	104.4369	-4203.44	4775.00
233	4.1942	4	6.1072	49.77	-140.43	31.8586	104.4158	-3350.40	4088.58
234	4.2008	4	9.1609	49.77	-140.43	31.8733	104.3946	-2639.88	3442.75
235	4.2228	4	12.2145	49.77	-140.43	31.8880	104.3734	-2202.11	2861.61
236	4.2652	4	15.2681	49.77	-140.45	31.9026	104.3521	-1960.38	2331.07
237	4.3361	4	18.3217	49.77	-129.65	31.9171	104.3308	-1817.58	1915.74
238	4.4499	4	21.3753	49.77	-129.35	31.9315	104.3092	-1769.82	1652.21
239	4.2004	4	3.0531	49.75	-140.43	31.8147	104.4086	-4991.87	5596.42
240	3.8958	4	6.1062	49.75	-140.97	31.8303	104.3885	-3820.50	4394.59
241	3.5782	4	9.1592	49.75	-141.66	31.8458	104.3684	-3078.96	3688.54
242	3.2442	4	12.2123	49.75	-142.56	31.8611	104.3481	-2631.09	3114.12
243	2.8885	4	15.2654	49.75	-143.83	31.8763	104.3278	-2342.42	2564.45
244	3.0320	4	18.3185	49.75	-129.65	31.8970	104.3079	-2133.25	2118.13
245	2.8591	4	21.3715	49.75	-129.35	31.9119	104.2871	-2018.22	1827.85
246	3.7265	4	3.0525	49.74	-126.81	31.7939	104.3833	-4437.94	4609.13
247	3.4212	4	6.1051	49.74	-126.20	31.8117	104.3660	-3846.31	4016.88
248	3.1047	4	9.1576	49.74	-125.41	31.8296	104.3488	-3350.07	3546.41
249	2.7741	4	12.2101	49.74	-124.35	31.8476	104.3318	-2972.06	3059.13
250	2.4254	4	15.2627	49.74	-122.84	31.8657	104.3152	-2661.29	2549.33
251	3.0323	4	18.3152	49.74	-129.64	31.8797	104.2832	-2417.59	2126.26
252	2.8594	4	21.3677	49.74	-129.34	31.8956	104.2637	-2244.52	1859.10
253	3.7263	4	3.0520	49.73	-126.79	31.7738	104.3518	-4060.60	3938.47
254	3.7251	4	6.1040	49.73	-126.79	31.7925	104.3354	-3830.42	3574.42
255	3.7377	4	9.1560	49.73	-126.79	31.8111	104.3191	-3561.06	3228.79
256	3.7680	4	12.2080	49.73	-126.78	31.8298	104.3028	-3253.11	2803.34

257	3.8222	4	15.2599	49.73	-126.76	31.8486	104.2867	-2919.29	2341.85
258	3.0326	4	18.3119	49.73	-129.64	31.8623	104.2585	-2618.57	1972.76
259	2.8597	4	21.3639	49.73	-129.32	31.8793	104.2403	-2400.38	1767.63
260	3.7283	4	3.0514	49.72	-126.79	31.7538	104.3202	-3733.45	3460.58
261	3.7273	4	6.1029	49.72	-126.79	31.7724	104.3038	-3692.33	3156.05
262	3.7262	4	9.1543	49.72	-126.79	31.7910	104.2874	-3567.80	2802.25
263	3.7252	4	12.2058	49.72	-126.79	31.8097	104.2711	-3316.84	2383.54
264	3.7244	4	15.2572	49.72	-126.79	31.8283	104.2547	-2989.08	1985.01
265	3.0330	4	18.3087	49.72	-126.79	31.8449	104.2338	-2674.18	1717.62
266	2.8923	4	21.3601	49.72	-126.78	31.8629	104.2167	-2450.23	1601.82
267	3.7274	4	3.0509	49.71	-126.78	31.7337	104.2887	-3399.84	3140.20
268	3.7265	4	6.1018	49.71	-126.78	31.7523	104.2723	-3401.95	2829.63
269	3.7257	4	9.1527	49.71	-126.78	31.7710	104.2559	-3324.73	2413.22
270	3.7249	4	12.2036	49.71	-126.78	31.7896	104.2395	-3117.87	1976.21
271	3.7241	4	15.2545	49.71	-126.78	31.8082	104.2231	-2839.45	1633.27
272	3.7233	4	18.3054	49.71	-126.77	31.8269	104.2067	-2576.48	1453.72
273	3.7224	4	21.3563	49.71	-126.77	31.8455	104.1903	-2391.63	1425.28
274	3.7286	4	3.0504	49.69	-126.79	31.7136	104.2571	-3065.98	2955.58
275	3.7275	4	6.1007	49.69	-126.79	31.7323	104.2407	-3017.10	2632.17
276	3.7265	4	9.1511	49.69	-126.79	31.7509	104.2243	-2917.39	2168.86
277	3.7255	4	12.2014	49.69	-126.78	31.7695	104.2079	-2744.09	1723.06
278	3.7245	4	15.2518	49.69	-126.78	31.7882	104.1915	-2540.51	1419.21
279	3.7235	4	18.3021	49.69	-126.78	31.8068	104.1752	-2363.40	1295.72
280	3.7224	4	21.3525	49.69	-126.78	31.8255	104.1588	-2252.62	1316.74
281	3.7284	4	3.0498	49.68	-126.77	31.6936	104.2255	-2777.98	2888.43
282	3.7272	4	6.0996	49.68	-126.77	31.7122	104.2092	-2645.92	2574.56
283	3.7260	4	9.1494	49.68	-126.77	31.7309	104.1928	-2501.12	2116.40
284	3.7248	4	12.1993	49.68	-126.76	31.7495	104.1764	-2352.38	1680.81
285	3.7235	4	15.2491	49.68	-126.76	31.7681	104.1600	-2218.90	1394.35
286	3.7223	4	18.2989	49.68	-126.76	31.7868	104.1436	-2125.36	1284.74
287	3.7211	4	21.3487	49.68	-126.76	31.8054	104.1272	-2088.80	1309.23
288	3.7303	4	3.0493	49.67	-126.77	31.6735	104.1940	-2586.89	2912.69
289	3.7293	4	6.0985	49.67	-126.77	31.6922	104.1776	-2406.89	2629.57
290	3.7283	4	9.1478	49.67	-126.77	31.7108	104.1612	-2223.95	2214.92
291	3.7278	4	12.1971	49.67	-126.76	31.7295	104.1448	-2078.12	1806.89
292	3.7291	4	15.2463	49.67	-126.76	31.7481	104.1284	-1983.67	1524.69
293	3.7335	4	18.2956	49.67	-126.76	31.7667	104.1120	-1943.05	1398.87
294	3.7426	4	21.3449	49.67	-126.76	31.7854	104.0956	-1955.33	1394.08
295	3.7294	4	3.0487	49.66	-126.76	31.6534	104.1624	-2499.76	2984.46
296	3.7286	4	6.0975	49.66	-126.76	31.6721	104.1460	-2309.59	2742.41
297	3.7904	4	9.1462	49.66	-126.78	31.6906	104.1294	-2112.28	2380.82
298	3.9060	4	12.1949	49.66	-126.85	31.7089	104.1125	-1962.80	2010.99
299	4.0683	4	15.2436	49.66	-126.99	31.7270	104.0954	-1879.40	1731.70

DOI: 10.1038/NGEO636

300	4.2710	4	18.2924	49.66	-127.20	31.7450	104.0781	-1856.90	1579.56
301	4.5092	4	21.3411	49.66	-127.46	31.7628	104.0605	-1886.42	1534.87
302	3.7306	4	3.0482	49.64	-126.76	31.6334	104.1308	-2487.78	3053.80
303	4.0654	4	6.2487	49.64	-129.53	31.6497	104.1127	-2310.61	2863.37
304	4.4245	4	9.3730	49.64	-131.92	31.6657	104.0941	-2123.86	2553.67
305	4.8083	4	12.4973	49.64	-133.99	31.6814	104.0751	-1984.73	2221.23
306	5.2163	4	15.6217	49.64	-135.80	31.6968	104.0558	-1907.62	1947.88
307	5.6481	4	18.7460	49.64	-137.39	31.7119	104.0363	-1883.74	1773.48
308	6.1034	4	21.8703	49.64	-138.80	31.7267	104.0164	-1899.68	1691.82
309	7.2189	4	3.2761	54.99	-143.51	31.5908	104.0893	-2521.42	3097.34
310	7.3690	4	6.3928	54.99	-144.34	31.6052	104.0711	-2367.57	2965.66
311	7.4575	4	9.5891	54.99	-145.29	31.6193	104.0526	-2209.16	2703.90
312	7.4914	4	12.7855	54.99	-146.34	31.6331	104.0337	-2093.28	2400.16
313	7.4765	4	15.9819	54.99	-147.48	31.6465	104.0146	-2019.34	2129.58
314	7.4170	4	19.1783	54.99	-148.71	31.6597	103.9951	-1978.55	1938.07
315	7.3160	4	22.3746	54.99	-150.06	31.6725	103.9755	-1960.27	1827.31
316	4.2855	4	3.2649	54.71	-132.39	31.5548	104.0530	-2563.47	2980.46
317	4.2999	4	6.5297	54.71	-132.22	31.5687	104.0350	-2448.45	2885.40
318	4.2904	4	9.7945	54.71	-131.99	31.5825	104.0170	-2320.82	2691.63
319	4.2555	4	13.0594	54.71	-131.68	31.5964	103.9990	-2207.97	2432.73
320	4.1936	4	16.3242	54.71	-131.27	31.6103	103.9811	-2112.62	2185.86
321	4.1035	4	19.5890	54.71	-130.75	31.6241	103.9632	-2041.11	2005.00
322	3.9837	4	22.8539	54.71	-130.07	31.6380	103.9454	-1999.96	1899.63
323	5.6041	4	3.2536	54.43	-144.11	31.5183	104.0155	-2617.65	2841.95
324	5.7829	4	6.5071	54.43	-143.74	31.5317	103.9967	-2556.68	2770.30
325	5.9605	4	9.7606	54.43	-143.38	31.5452	103.9780	-2451.58	2613.47
326	6.1381	4	13.0142	54.43	-143.04	31.5587	103.9593	-2329.23	2381.95
327	6.3174	4	16.2677	54.43	-142.71	31.5723	103.9408	-2209.20	2158.13
328	6.5002	4	19.5212	54.43	-142.39	31.5860	103.9223	-2108.91	2001.35
329	6.6887	4	22.7748	54.43	-142.06	31.5997	103.9039	-2039.84	1922.43
330	4.1378	4	3.2422	54.15	-141.40	31.4843	103.9852	-2644.33	2671.96
331	4.0819	4	6.4843	54.15	-141.17	31.4973	103.9657	-2590.39	2589.98
332	4.0294	4	9.7265	54.15	-140.94	31.5104	103.9464	-2489.15	2445.00
333	3.9799	4	12.9687	54.15	-140.71	31.5235	103.9271	-2358.98	2254.68
334	3.9331	4	16.2108	54.15	-140.47	31.5368	103.9079	-2226.76	2082.93
335	3.8887	4	19.4530	54.15	-140.24	31.5501	103.8887	-2116.88	1973.45
336	3.8467	4	22.6952	54.15	-140.00	31.5635	103.8696	-2042.88	1930.15
337	4.1383	4	3.2307	53.87	-141.39	31.4553	103.9578	-2666.85	2509.11
338	4.1180	4	6.4614	53.87	-141.18	31.4686	103.9385	-2601.16	2415.07
339	4.0993	4	9.6921	53.87	-140.97	31.4821	103.9192	-2476.70	2280.04
340	4.0821	4	12.9229	53.87	-140.77	31.4955	103.9000	-2326.60	2126.78
341	4.0665	4	16.1536	53.87	-140.56	31.5091	103.8809	-2186.29	2006.31
342	4.0524	4	19.3843	53.87	-140.34	31.5227	103.8618	-2078.42	1945.93

343	4.0400	4	22.6150	53.87	-140.13	31.5363	103.8427	-2011.69	1941.73
344	5.5323	4	3.2192	53.59	-140.45	31.4219	103.9258	-2688.18	2371.55
345	5.5118	4	6.4384	53.59	-140.29	31.4355	103.9065	-2586.69	2250.03
346	5.4929	4	9.6576	53.59	-140.14	31.4491	103.8872	-2407.95	2134.88
347	5.4758	4	12.8767	53.59	-139.98	31.4628	103.8680	-2230.64	2033.94
348	5.4604	4	16.0959	53.59	-139.82	31.4765	103.8488	-2091.75	1969.39
349	5.4468	4	19.3151	53.59	-139.67	31.4902	103.8296	-2000.10	1954.71
350	5.4350	4	22.5343	53.59	-139.51	31.5041	103.8105	-1954.08	1984.76
351	5.5323	4	3.2076	53.31	-140.43	31.3837	103.8885	-2671.15	2281.57
352	5.4498	4	6.4152	53.31	-140.30	31.3977	103.8695	-2478.46	2155.20
353	5.3652	4	9.6227	53.31	-140.18	31.4117	103.8504	-2255.07	2100.93
354	5.2784	4	12.8303	53.31	-140.05	31.4258	103.8314	-2082.81	2069.04
355	5.1891	4	16.0379	53.31	-139.93	31.4399	103.8124	-1972.16	2051.01
356	5.0973	4	19.2455	53.31	-139.80	31.4541	103.7935	-1912.51	2057.50
357	5.0025	4	22.4531	53.31	-139.68	31.4684	103.7747	-1893.29	2091.02
358	4.0437	4	3.1959	53.03	-136.55	31.3525	103.8564	-2544.55	2361.13
359	3.9616	4	6.3918	53.03	-136.30	31.3671	103.8378	-2304.49	2262.70
360	3.8778	4	9.5877	53.03	-136.03	31.3819	103.8192	-2090.32	2264.59
361	3.7923	4	12.7836	53.03	-135.76	31.3967	103.8008	-1954.40	2267.11
362	3.7050	4	15.9795	53.03	-135.48	31.4115	103.7824	-1881.08	2254.33
363	3.6160	4	19.1754	53.03	-135.19	31.4265	103.7640	-1849.83	2244.79
364	3.5252	4	22.3713	53.03	-134.88	31.4414	103.7458	-1848.53	2251.84
365	4.0441	4	3.1842	52.75	-136.52	31.3262	103.8270	-2361.49	2639.48
366	4.0431	4	6.3683	52.75	-136.31	31.3412	103.8085	-2142.08	2556.16
367	4.0433	4	9.5524	52.75	-136.10	31.3563	103.7902	-1974.08	2573.09
368	4.0447	4	12.7366	52.75	-135.89	31.3715	103.7719	-1879.95	2565.81
369	4.0476	4	15.9207	52.75	-135.68	31.3867	103.7536	-1836.92	2520.58
370	4.0522	4	19.1048	52.75	-135.47	31.4020	103.7354	-1822.42	2467.99
371	4.0589	4	22.2890	52.75	-135.26	31.4173	103.7173	-1827.60	2434.88
372	4.0448	4	3.1723	52.47	-136.53	31.2999	103.7976	-2290.25	3058.44
373	4.0720	4	6.3446	52.47	-136.33	31.3149	103.7789	-2131.91	2961.90
374	4.0998	4	9.5169	52.47	-136.13	31.3300	103.7603	-1985.04	2955.07
375	4.1283	4	12.6892	52.47	-135.93	31.3452	103.7418	-1902.43	2913.39
376	4.1573	4	15.8615	52.47	-135.73	31.3604	103.7233	-1862.96	2811.83
377	4.1870	4	19.0339	52.47	-135.53	31.3756	103.7049	-1841.69	2697.62
378	4.2175	4	22.2062	52.47	-135.34	31.3909	103.6865	-1833.48	2614.02
379	4.6425	4	3.1604	52.20	-137.82	31.2709	103.7660	-2311.23	3537.52
380	4.6688	4	6.3208	52.20	-137.64	31.2859	103.7471	-2222.46	3352.27
381	4.7021	4	9.4812	52.20	-137.46	31.3009	103.7281	-2088.50	3323.25
382	4.7407	4	12.6416	52.20	-137.28	31.3159	103.7092	-2001.26	3245.92
383	4.7835	4	15.8020	52.20	-137.10	31.3309	103.6904	-1942.95	3077.98
384	4.8299	4	18.9624	52.20	-136.93	31.3460	103.6715	-1892.44	2893.52
385	4.8800	4	22.1228	52.20	-136.75	31.3612	103.6528	-1851.90	2757.61

DOI: 10.1038/NGEO636

386	4.6423	4	3.1484	51.92	-137.81	31.2401	103.7331	-2281.87	4102.40
387	4.8877	4	6.2968	51.92	-137.93	31.2541	103.7131	-2227.30	3818.88
388	5.1065	4	9.4453	51.92	-137.97	31.2682	103.6931	-2157.73	3714.68
389	5.3037	4	12.5937	51.92	-137.97	31.2824	103.6733	-2096.21	3549.36
390	5.4874	4	15.7421	51.92	-134.25	31.2967	103.6535	-2022.53	3290.36
391	5.6728	4	18.8905	51.92	-132.32	31.3110	103.6338	-1934.34	3028.61
392	5.8895	4	22.0389	51.92	-131.34	31.3253	103.6139	-1853.05	2841.50
393	7.0873	4	3.1364	51.64	-149.26	31.1938	103.6945	-2210.47	4793.06
394	6.8741	4	6.0175	51.64	-147.83	31.2086	103.6738	-2161.99	4487.07
395	6.5470	4	9.0262	51.64	-146.64	31.2240	103.6537	-2163.14	4204.19
396	6.0881	4	12.0349	51.64	-145.83	31.2397	103.6343	-2128.52	3855.41
397	3.6678	4	15.6819	51.64	-134.24	31.2692	103.6226	-2044.37	3459.15
398	3.0198	4	18.8183	51.64	-130.45	31.2858	103.6048	-1922.27	3105.97
399	2.2549	4	21.9547	51.64	-126.72	31.3022	103.5876	-1805.73	2853.37
400	3.7050	4	2.7414	43.26	-130.87	31.1639	103.6631	-2402.58	5399.56
401	3.3240	4	5.7461	43.26	-126.07	31.1829	103.6445	-2358.21	5050.42
402	2.9997	4	8.6191	43.26	-120.37	31.2029	103.6275	-2276.31	4605.85
403	2.7320	4	11.4922	43.26	-113.67	31.2236	103.6125	-2169.10	4105.50
404	3.6683	4	13.7069	43.26	-105.83	31.2489	103.5918	-2042.24	3584.10
405	3.5111	4	16.4483	43.26	-96.49	31.2698	103.5767	-1869.87	3110.58
406	3.0272	4	19.1896	43.26	-84.70	31.2916	103.5648	-1695.14	2750.68
407	3.7055	4	2.7414	43.26	-130.86	31.1421	103.6337	-2631.71	5871.93
408	3.7044	4	5.4828	43.26	-130.87	31.1619	103.6137	-2534.43	5441.83
409	3.8253	4	8.2241	43.26	-130.80	31.1820	103.5942	-2336.63	4893.87
410	4.0901	4	10.9655	43.26	-130.48	31.2027	103.5754	-2131.17	4300.23
411	4.5211	4	13.7069	43.26	-129.70	31.2238	103.5577	-1933.26	3674.99
412	5.1415	4	16.4483	43.26	-128.32	31.2455	103.5414	-1721.31	3067.09
413	5.9781	4	19.1896	43.26	-126.24	31.2678	103.5269	-1477.42	2494.98
414	3.7060	4	2.7414	43.26	-130.85	31.1203	103.6043	-2810.67	6046.85
415	3.7052	4	5.4828	43.26	-130.86	31.1401	103.5842	-2569.51	5594.28
416	3.7044	4	8.2241	43.26	-130.87	31.1599	103.5642	-2280.26	5013.42
417	3.7056	4	10.9655	43.26	-130.88	31.1797	103.5442	-2007.00	4390.99
418	3.7153	4	13.7069	43.26	-130.89	31.1995	103.5242	-1761.62	3730.45
419	3.7451	4	16.4483	43.26	-130.90	31.2194	103.5042	-1531.39	3074.99
420	3.8101	4	19.1896	43.26	-130.89	31.2394	103.4844	-1298.20	2453.94
421	3.7072	4	2.7414	43.26	-130.86	31.0985	103.5748	-2841.94	5864.97
422	3.7061	4	5.4828	43.26	-130.87	31.1183	103.5548	-2515.21	5514.85
423	3.7050	4	8.2241	43.26	-130.88	31.1381	103.5348	-2145.27	4993.11
424	3.7039	4	10.9655	43.26	-130.89	31.1579	103.5147	-1819.75	4401.28
425	3.7027	4	13.7069	43.26	-130.90	31.1777	103.4947	-1552.79	3760.75
426	3.7016	4	16.4483	43.26	-130.91	31.1975	103.4746	-1330.97	3108.54
427	3.7007	4	19.1896	43.26	-130.92	31.2173	103.4546	-1129.13	2482.70
428	3.7069	4	2.7414	43.26	-130.84	31.0767	103.5454	-2684.07	5448.26

429	3.7055	4	5.4828	43.26	-130.85	31.0965	103.5254	-2348.64	5210.22
430	3.7041	4	8.2241	43.26	-130.86	31.1163	103.5054	-1939.87	4814.56
431	3.7026	4	10.9655	43.26	-130.87	31.1361	103.4853	-1587.98	4326.87
432	3.7012	4	13.7069	43.26	-130.88	31.1559	103.4653	-1327.02	3763.83
433	3.6998	4	16.4483	43.26	-130.89	31.1757	103.4453	-1136.29	3152.06
434	3.6983	4	19.1896	43.26	-130.90	31.1955	103.4252	-976.18	2537.38
435	3.7074	4	2.7414	43.26	-130.83	31.0549	103.5160	-2421.59	4900.14
436	3.7061	4	5.4828	43.26	-130.84	31.0747	103.4960	-2094.99	4760.89
437	3.7047	4	8.2241	43.26	-130.85	31.0945	103.4760	-1692.24	4516.16
438	3.7034	4	10.9655	43.26	-130.86	31.1143	103.4559	-1355.86	4183.00
439	3.7020	4	13.7069	43.26	-130.87	31.1341	103.4359	-1129.78	3738.16
440	3.7007	4	16.4483	43.26	-130.89	31.1539	103.4159	-981.73	3188.30
441	3.6993	4	19.1896	43.26	-130.90	31.1737	103.3958	-859.57	2591.22
442	3.7086	4	2.7414	43.26	-130.82	31.0331	103.4865	-2118.41	4285.99
443	3.7075	4	5.4828	43.26	-130.83	31.0529	103.4665	-1824.40	4235.36
444	3.7064	4	8.2241	43.26	-130.84	31.0727	103.4465	-1465.18	4147.55
445	3.7053	4	10.9655	43.26	-130.85	31.0925	103.4265	-1180.67	3988.46
446	3.7042	4	13.7069	43.26	-130.86	31.1123	103.4065	-1007.23	3674.47
447	3.7031	4	16.4483	43.26	-130.87	31.1321	103.3865	-897.26	3191.71
448	3.7020	4	19.1896	43.26	-130.88	31.1519	103.3664	-794.30	2617.00
449	3.7084	4	2.7414	43.26	-130.82	31.0113	103.4571	-1841.02	3671.79
450	3.7075	4	5.4828	43.26	-130.83	31.0311	103.4371	-1603.19	3686.49
451	3.7067	4	8.2241	43.26	-130.84	31.0509	103.4171	-1311.92	3743.79
452	3.7058	4	10.9655	43.26	-130.85	31.0707	103.3971	-1098.74	3751.69
453	3.7050	4	13.7069	43.26	-130.86	31.0905	103.3771	-978.89	3555.09
454	3.7041	4	16.4483	43.26	-130.87	31.1103	103.3571	-888.89	3132.75
455	3.7032	4	19.1896	43.26	-130.88	31.1301	103.3370	-779.41	2588.59
456	3.7089	4	2.7414	43.26	-130.81	30.9895	103.4277	-1634.40	3105.11
457	3.7078	4	5.4828	43.26	-130.82	31.0093	103.4077	-1489.13	3148.60
458	3.7067	4	8.2241	43.26	-130.83	31.0291	103.3877	-1280.71	3318.46
459	3.7056	4	10.9655	43.26	-130.84	31.0489	103.3677	-1133.01	3465.02
460	3.7045	4	13.7069	43.26	-130.86	31.0687	103.3477	-1042.37	3356.61
461	3.7034	4	16.4483	43.26	-130.87	31.0885	103.3277	-941.84	2986.46
462	3.7023	4	19.1896	43.26	-130.88	31.1084	103.3076	-800.04	2488.30
463	3.7094	4	2.7414	43.26	-130.81	30.9677	103.3982	-1492.15	2623.58
464	3.7086	4	5.4828	43.26	-130.82	30.9875	103.3782	-1485.17	2648.89
465	3.7078	4	8.2241	43.26	-130.83	31.0073	103.3583	-1370.44	2870.37
466	3.7070	4	10.9655	43.26	-130.84	31.0271	103.3383	-1264.73	3107.05
467	3.7063	4	13.7069	43.26	-130.85	31.0469	103.3183	-1165.39	3057.42
468	3.7055	4	16.4483	43.26	-130.86	31.0668	103.2983	-1024.66	2741.43
469	3.7047	4	19.1896	43.26	-130.87	31.0866	103.2782	-834.07	2313.64
470	3.7106	4	2.7414	43.26	-130.81	30.9459	103.3688	-1358.42	2253.09
471	3.7095	4	5.4828	43.26	-130.82	30.9657	103.3488	-1457.16	2227.95

DOI: 10.1038/NGEO636

472	3.7084	4	8.2241	43.26	-130.83	30.9855	103.3288	-1445.83	2432.02
473	3.7073	4	10.9655	43.26	-130.84	31.0053	103.3089	-1384.57	2688.88
474	3.7062	4	13.7069	43.26	-130.86	31.0251	103.2889	-1270.26	2669.90
475	3.7051	4	16.4483	43.26	-130.87	31.0450	103.2689	-1089.43	2415.41
476	3.7040	4	19.1896	43.26	-130.88	31.0648	103.2488	-856.95	2082.69
477	3.7103	4	2.7414	43.26	-130.79	30.9241	103.3394	-1214.59	1971.10
478	3.7089	4	5.4828	43.26	-130.80	30.9439	103.3194	-1325.28	1908.31
479	3.7075	4	8.2241	43.26	-130.82	30.9637	103.2994	-1364.43	2087.44
480	3.7060	4	10.9655	43.26	-130.83	30.9835	103.2795	-1362.38	2291.80
481	3.7046	4	13.7069	43.26	-130.84	31.0034	103.2595	-1270.27	2264.98
482	3.7032	4	16.4483	43.26	-130.85	31.0232	103.2395	-1088.16	2064.98
483	3.7017	4	19.1896	43.26	-130.86	31.0430	103.2195	-848.87	1835.23
484	3.7108	4	2.7414	43.26	-130.79	30.9023	103.3099	-1097.97	1703.31
485	3.7097	4	5.4828	43.26	-130.80	30.9221	103.2900	-1096.68	1665.58
486	3.7085	4	8.2241	43.26	-130.81	30.9419	103.2700	-1131.81	1875.75
487	3.7073	4	10.9655	43.26	-130.82	30.9617	103.2500	-1181.20	2005.82
488	3.7060	4	13.7069	43.26	-130.83	30.9816	103.2301	-1142.70	1938.14
489	3.7047	4	16.4483	43.26	-130.84	31.0014	103.2101	-1006.11	1770.66
490	3.7032	4	19.1896	43.26	-130.85	31.0212	103.1901	-808.33	1626.01
491	3.7113	4	2.7414	43.26	-130.78	30.8805	103.2805	-916.92	1508.46
492	3.7105	4	5.4828	43.26	-130.79	30.9003	103.2605	-856.30	1628.41
493	3.7097	4	8.2241	43.26	-130.80	30.9201	103.2406	-911.07	1796.81
494	3.7089	4	10.9655	43.26	-130.80	30.9400	103.2206	-969.98	1842.00
495	3.7079	4	13.7069	43.26	-130.81	30.9598	103.2007	-966.24	1747.66
496	3.7069	4	16.4483	43.26	-130.82	30.9796	103.1807	-890.61	1610.08
497	3.7059	4	19.1896	43.26	-130.83	30.9994	103.1607	-771.13	1514.30
498	3.8829	4	1.8614	27.73	-136.29	31.5229	104.1849	-1111.82	2491.06
499	3.8819	4	3.7228	27.73	-136.30	31.5449	104.1579	-941.57	2239.43
500	3.8811	4	5.5841	27.73	-136.31	31.5669	104.1309	-812.54	2008.00
501	3.8803	4	7.4455	27.73	-136.32	31.5889	104.1039	-729.56	1842.92
502	3.8797	4	9.3069	27.73	-136.33	31.6109	104.0768	-688.35	1752.26
503	3.8819	4	1.8614	27.73	-136.28	31.4977	104.1566	-995.30	2359.00
504	3.8805	4	3.7228	27.73	-136.29	31.5197	104.1296	-876.17	2154.16
505	3.8793	4	5.5841	27.73	-136.31	31.5417	104.1026	-777.79	1941.36
506	3.8781	4	7.4455	27.73	-136.32	31.5637	104.0756	-713.58	1784.01
507	3.8770	4	9.3069	27.73	-136.34	31.5856	104.0486	-686.80	1707.30
508	3.8839	4	1.8614	27.73	-136.27	31.4724	104.1284	-888.11	2265.69
509	3.8825	4	3.7228	27.73	-136.29	31.4944	104.1014	-818.50	2082.80
510	3.8811	4	5.5841	27.73	-136.30	31.5164	104.0744	-759.99	1885.66
511	3.8797	4	7.4455	27.73	-136.32	31.5384	104.0474	-721.89	1737.28
512	3.8783	4	9.3069	27.73	-136.33	31.5604	104.0203	-708.25	1668.36
513	3.8829	4	1.8614	27.73	-136.26	31.4472	104.1001	-822.86	2191.51
514	3.8815	4	3.7228	27.73	-136.28	31.4692	104.0731	-788.27	2021.82

515	3.8801	4	5.5841	27.73	-136.29	31.4912	104.0461	-761.98	1837.87
516	3.8788	4	7.4455	27.73	-136.31	31.5132	104.0191	-748.10	1699.69
517	3.8774	4	9.3069	27.73	-136.32	31.5352	103.9921	-744.72	1634.81
518	3.8849	4	1.8614	27.73	-136.26	31.4220	104.0718	-785.29	2095.79
519	3.8835	4	3.7228	27.73	-136.27	31.4440	104.0448	-776.17	1947.40
520	3.8821	4	5.5841	27.73	-136.29	31.4660	104.0178	-774.16	1785.00
521	3.8807	4	7.4455	27.73	-136.30	31.4880	103.9909	-776.89	1661.15
522	3.8793	4	9.3069	27.73	-136.31	31.5100	103.9638	-777.76	1599.56
523	3.8839	4	1.8614	27.73	-136.25	31.3967	104.0435	-728.17	1975.93
524	3.8825	4	3.7228	27.73	-136.26	31.4188	104.0166	-759.19	1856.68
525	3.8812	4	5.5841	27.73	-136.28	31.4408	103.9896	-785.41	1721.70
526	3.8800	4	7.4455	27.73	-136.29	31.4628	103.9626	-800.41	1612.15
527	3.8788	4	9.3069	27.73	-136.31	31.4848	103.9356	-798.00	1553.80
528	3.8859	4	1.8614	27.73	-136.24	31.3715	104.0152	-628.41	1874.96
529	3.9093	4	3.7228	27.73	-136.26	31.3934	103.9882	-732.36	1768.90
530	3.9327	4	5.5841	27.73	-136.28	31.4154	103.9611	-789.48	1655.34
531	3.9559	4	7.4455	27.73	-136.29	31.4373	103.9341	-810.90	1551.48
532	3.9791	4	9.3069	27.73	-136.31	31.4592	103.9070	-795.76	1493.05
533	3.8733	4	1.8614	27.73	-137.04	31.3458	103.9868	-669.05	1757.55
534	3.8970	4	3.7228	27.73	-137.05	31.3676	103.9596	-724.59	1690.30
535	3.9207	4	5.5841	27.73	-137.06	31.3894	103.9324	-776.59	1593.78
536	3.9443	4	7.4455	27.73	-137.07	31.4111	103.9052	-785.10	1481.93
537	3.9678	4	9.3069	27.73	-137.08	31.4329	103.8779	-751.83	1421.88
538	3.8732	4	1.8614	27.73	-137.04	31.3203	103.9591	-661.12	1688.74
539	3.8718	4	3.7228	27.73	-137.05	31.3420	103.9318	-687.61	1640.77
540	3.8705	4	5.5841	27.73	-137.07	31.3637	103.9045	-719.28	1545.70
541	3.8693	4	7.4455	27.73	-137.08	31.3854	103.8772	-708.00	1415.44
542	3.8681	4	9.3069	27.73	-137.10	31.4071	103.8498	-668.70	1358.73
543	3.8743	4	1.8614	27.73	-137.02	31.2949	103.9313	-641.46	1664.19
544	3.8733	4	3.7228	27.73	-137.04	31.3165	103.9040	-631.61	1618.09
545	3.8723	4	5.5841	27.73	-137.05	31.3382	103.8767	-627.59	1519.57
546	3.8712	4	7.4455	27.73	-137.06	31.3599	103.8494	-601.33	1377.49
547	3.8702	4	9.3069	27.73	-137.08	31.3816	103.8221	-575.92	1327.93
548	3.8750	4	1.8614	27.73	-137.04	31.2694	103.9035	-637.66	1679.90
549	3.8736	4	3.7228	27.73	-137.05	31.2910	103.8762	-600.81	1622.13
550	3.8722	4	5.5841	27.73	-137.06	31.3127	103.8490	-566.66	1521.56
551	3.8708	4	7.4455	27.73	-137.08	31.3344	103.8217	-531.48	1386.96
552	3.8695	4	9.3069	27.73	-137.09	31.3561	103.7944	-524.69	1345.07
553	3.8753	4	1.8614	27.73	-137.01	31.2439	103.8757	-671.96	1744.40
554	3.8736	4	3.7228	27.73	-137.02	31.2656	103.8485	-632.75	1670.17
555	3.8718	4	5.5841	27.73	-137.03	31.2873	103.8212	-605.71	1564.57
556	3.8706	4	7.4455	27.73	-127.35	31.3090	103.7939	-573.35	1442.61
557	3.8730	4	9.3069	27.73	-127.46	31.3306	103.7666	-558.12	1402.72

DOI: 10.1038/NGEO636

558	3.8751	4	1.8614	27.73	-137.01	31.2184	103.8480	-740.63	1841.56
559	3.8737	4	3.7228	27.73	-137.02	31.2401	103.8207	-709.88	1766.02
560	3.9343	4	5.5841	27.73	-137.05	31.2616	103.7932	-708.52	1656.23
561	2.6902	4	7.4455	27.73	-127.35	31.2925	103.7735	-689.07	1524.37
562	2.3688	4	9.3069	27.73	-127.46	31.3150	103.7475	-658.50	1473.50
563	3.8762	4	1.8614	27.73	-136.99	31.1929	103.8202	-840.40	1957.88
564	3.2525	4	3.7228	27.73	-139.01	31.2155	103.7948	-801.13	1880.44
565	2.5731	4	5.5841	27.73	-142.67	31.2370	103.7686	-802.69	1764.31
566	2.6905	4	7.4455	27.73	-127.34	31.2778	103.7510	-801.81	1607.15
567	2.3690	4	9.3069	27.73	-127.46	31.3021	103.7277	-762.80	1547.88
568	3.5392	4	1.8614	27.73	-116.34	31.1799	103.8003	-956.05	2037.86
569	2.9154	4	3.7228	27.73	-114.11	31.2073	103.7825	-915.24	1977.11
570	2.2436	4	5.5841	27.73	-109.95	31.2350	103.7662	-905.44	1858.66
571	2.6908	4	7.4455	27.73	-127.34	31.2631	103.7285	-884.33	1694.73
572	2.3692	4	9.3069	27.73	-127.07	31.2891	103.7079	-846.32	1629.59
573	3.5391	4	1.8614	27.73	-116.32	31.1658	103.7670	-1026.25	2131.68
574	3.5378	4	3.7228	27.73	-116.33	31.1943	103.7505	-974.28	2080.89
575	3.6056	4	5.5841	27.73	-116.31	31.2230	103.7343	-950.38	1965.20
576	2.6910	4	7.4455	27.73	-116.16	31.2485	103.7060	-919.99	1793.80
577	2.5409	4	9.3069	27.73	-115.19	31.2759	103.6876	-897.56	1717.69
578	3.5400	4	1.8614	27.73	-116.33	31.1517	103.7337	-1043.69	2190.75
579	3.5396	4	3.7228	27.73	-116.34	31.1802	103.7172	-994.76	2134.62
580	3.5392	4	5.5841	27.73	-116.34	31.2087	103.7007	-955.81	2024.63
581	3.5393	4	7.4455	27.73	-116.35	31.2373	103.6841	-932.00	1882.41
582	3.5444	4	9.3069	27.73	-116.36	31.2658	103.6676	-926.80	1795.24
583	5.9773	4	19.1896	0.00	-126.24	31.2968	103.5020	-1101.20	1637.32
584	6.2558	4	19.1896	0.00	-126.36	31.3250	103.4759	-897.38	1186.33
585	6.4078	4	19.1896	0.00	-126.43	31.3535	103.4502	-693.72	801.80
586	6.5553	4	19.1896	0.00	-126.48	31.3820	103.4246	-504.67	529.62
587	6.6988	4	19.1896	0.00	-126.54	31.4105	103.3989	-345.85	376.42
588	6.8386	4	19.1896	0.00	-126.59	31.4390	103.3732	-230.78	316.80
589	6.9751	4	19.1896	0.00	-126.64	31.4675	103.3474	-166.82	309.59
590	3.8098	4	19.1896	0.00	-130.90	31.2666	103.4569	-1039.10	1787.31
591	4.0898	4	19.1896	0.00	-130.76	31.2946	103.4305	-829.08	1252.93
592	4.2481	4	19.1896	0.00	-130.70	31.3223	103.4037	-637.49	832.79
593	4.4046	4	19.1896	0.00	-130.64	31.3500	103.3768	-462.14	544.03
594	4.5596	4	19.1896	0.00	-130.59	31.3777	103.3500	-312.52	384.98
595	4.7131	4	19.1896	0.00	-130.55	31.4054	103.3231	-201.61	326.03
596	4.8653	4	19.1896	0.00	-130.51	31.4331	103.2962	-139.78	322.16
597	3.6997	4	19.1896	0.00	-130.91	31.2445	103.4270	-913.40	1876.80
598	3.6993	4	19.1896	0.00	-130.94	31.2716	103.3995	-727.54	1339.79
599	3.7041	4	19.1896	0.00	-130.95	31.2988	103.3719	-559.43	907.12
600	3.7116	4	19.1896	0.00	-130.97	31.3260	103.3443	-404.67	603.84

601	3.7215	4	19.1896	0.00	-130.98	31.3532	103.3167	-269.51	429.98
602	3.7337	4	19.1896	0.00	-131.00	31.3804	103.2892	-166.06	357.78
603	3.7479	4	19.1896	0.00	-131.01	31.4076	103.2616	-106.17	344.14
604	3.6981	4	19.1896	0.00	-130.91	31.2227	103.3977	-783.39	1959.64
605	3.6957	4	19.1896	0.00	-130.93	31.2499	103.3701	-622.33	1432.05
606	3.6939	4	19.1896	0.00	-130.94	31.2770	103.3425	-477.11	993.27
607	3.6921	4	19.1896	0.00	-130.96	31.3042	103.3149	-340.46	674.72
608	3.6904	4	19.1896	0.00	-130.97	31.3313	103.2873	-217.26	482.43
609	3.6886	4	19.1896	0.00	-130.99	31.3585	103.2597	-120.21	393.77
610	3.6868	4	19.1896	0.00	-131.00	31.3856	103.2320	-63.33	369.72
611	3.6985	4	19.1896	0.00	-130.91	31.2009	103.3683	-681.42	2036.84
612	3.6957	4	19.1896	0.00	-130.92	31.2281	103.3407	-536.49	1521.88
613	3.6939	4	19.1896	0.00	-130.93	31.2553	103.3132	-404.75	1079.66
614	3.6920	4	19.1896	0.00	-130.95	31.2824	103.2856	-277.70	746.51
615	3.6902	4	19.1896	0.00	-130.96	31.3096	103.2580	-160.80	535.73
616	3.6883	4	19.1896	0.00	-130.98	31.3368	103.2304	-68.02	430.91
617	3.6865	4	19.1896	0.00	-130.99	31.3639	103.2027	-14.68	397.58
618	3.7019	4	19.1896	0.00	-130.88	31.1791	103.3389	-622.33	2091.99
619	3.6991	4	19.1896	0.00	-130.91	31.2063	103.3114	-479.84	1593.79
620	3.6974	4	19.1896	0.00	-130.92	31.2335	103.2838	-347.61	1152.21
621	3.6958	4	19.1896	0.00	-130.94	31.2607	103.2563	-219.47	809.02
622	3.6941	4	19.1896	0.00	-130.95	31.2878	103.2287	-102.99	584.61
623	3.6924	4	19.1896	0.00	-130.97	31.3150	103.2011	-12.96	467.99
624	3.6907	4	19.1896	0.00	-130.98	31.3422	103.1734	35.91	428.40
625	3.7024	4	19.1896	0.00	-130.88	31.1573	103.3095	-602.55	2104.59
626	3.7005	4	19.1896	0.00	-130.90	31.1845	103.2820	-447.55	1630.66
627	3.6993	4	19.1896	0.00	-130.92	31.2117	103.2545	-301.82	1198.15
628	3.6981	4	19.1896	0.00	-130.93	31.2389	103.2269	-164.62	854.73
629	3.6970	4	19.1896	0.00	-130.94	31.2661	103.1993	-45.66	626.25
630	3.6958	4	19.1896	0.00	-130.96	31.2932	103.1717	41.24	505.32
631	3.6946	4	19.1896	0.00	-130.97	31.3204	103.1441	84.16	463.51
632	3.7022	4	19.1896	0.00	-130.88	31.1356	103.2801	-607.20	2059.23
633	3.7001	4	19.1896	0.00	-130.90	31.1627	103.2526	-428.19	1620.78
634	3.6985	4	19.1896	0.00	-130.92	31.1899	103.2251	-261.48	1210.67
635	3.6969	4	19.1896	0.00	-130.93	31.2171	103.1975	-112.86	881.31
636	3.6953	4	19.1896	0.00	-130.95	31.2443	103.1700	7.49	661.03
637	3.6938	4	19.1896	0.00	-130.96	31.2714	103.1424	89.23	544.12
638	3.6922	4	19.1896	0.00	-130.98	31.2986	103.1148	124.95	503.68
639	3.7048	4	19.1896	0.00	-130.87	31.1138	103.2508	-619.60	1952.90
640	3.7037	4	19.1896	0.00	-130.89	31.1410	103.2232	-413.37	1562.89
641	3.7026	4	19.1896	0.00	-130.90	31.1681	103.1957	-226.03	1190.99
642	3.7015	4	19.1896	0.00	-130.92	31.1953	103.1682	-68.93	891.34
643	3.7004	4	19.1896	0.00	-130.93	31.2225	103.1406	49.50	691.18

DOI: 10.1038/NGEO636

644	3.6992	4	19.1896	0.00	-130.94	31.2497	103.1130	124.20	585.16
645	3.6981	4	19.1896	0.00	-130.96	31.2768	103.0854	152.90	548.30
646	3.7031	4	19.1896	0.00	-130.89	31.0920	103.2213	-625.32	1799.31
647	3.7013	4	19.1896	0.00	-130.90	31.1191	103.1938	-399.58	1468.03
648	3.7002	4	19.1896	0.00	-130.92	31.1463	103.1663	-199.90	1147.74
649	3.6991	4	19.1896	0.00	-130.93	31.1735	103.1388	-40.66	890.40
650	3.6979	4	19.1896	0.00	-130.95	31.2007	103.1112	72.64	718.95
651	3.6968	4	19.1896	0.00	-130.96	31.2279	103.0837	140.19	627.85
652	3.6957	4	19.1896	0.00	-130.97	31.2550	103.0561	164.13	595.15
653	3.7015	4	19.1896	0.00	-130.87	31.0702	103.1920	-611.65	1627.36
654	3.6980	4	19.1896	0.00	-130.89	31.0974	103.1645	-383.26	1357.43
655	3.6957	4	19.1896	0.00	-130.90	31.1246	103.1370	-185.53	1094.65
656	3.6934	4	19.1896	0.00	-130.91	31.1517	103.1095	-32.21	885.13
657	3.6912	4	19.1896	0.00	-130.93	31.1789	103.0819	73.75	745.48
658	3.6889	4	19.1896	0.00	-130.94	31.2061	103.0544	135.79	669.97
659	3.6867	4	19.1896	0.00	-130.96	31.2333	103.0268	158.57	640.74
660	3.7027	4	19.1896	0.00	-130.85	31.0484	103.1626	-569.20	1470.59
661	3.6995	4	19.1896	0.00	-130.87	31.0756	103.1352	-359.46	1256.64
662	3.6972	4	19.1896	0.00	-130.88	31.1028	103.1077	-180.22	1048.58
663	3.6947	4	19.1896	0.00	-130.90	31.1300	103.0801	-40.89	883.51
664	3.6921	4	19.1896	0.00	-130.91	31.1572	103.0526	56.41	772.02
665	3.6893	4	19.1896	0.00	-130.93	31.1844	103.0251	115.22	708.92
666	3.6865	4	19.1896	0.00	-130.94	31.2115	102.9975	140.54	681.01
667	3.7053	4	19.1896	0.00	-130.84	31.0266	103.1333	-491.72	1344.53
668	3.7034	4	19.1896	0.00	-130.85	31.0538	103.1058	-332.48	1189.41
669	3.7018	4	19.1896	0.00	-130.86	31.0811	103.0783	-183.79	1028.59
670	3.7002	4	19.1896	0.00	-130.87	31.1082	103.0508	-61.68	895.89
671	3.6984	4	19.1896	0.00	-130.88	31.1354	103.0233	28.18	801.45
672	3.6965	4	19.1896	0.00	-130.89	31.1626	102.9958	86.69	742.88
673	3.6944	4	19.1896	0.00	-130.90	31.1898	102.9682	118.19	711.64

*Length: fault patch horizontal length; depth: fault lower edge depth; dip: fault dip angle; strike: fault strike direction, clockwise from north; lat & long: coordinate of fault patch lower left corner; SS & TS: strike slip and thrust slip components in mm.

Table 3. GPS data fitting.

	Sites	Long	Lat	D	E/mm	Prd_E/mm	Sig_E/mm	N/mm	Prd_N/mm	Sig_N/mm	U/mm	Prd_U/mm	Sig_U/mm*
1	1375	105.815	33.340	18	5.0	16.1	8.0	42.0	64.4	8.0			
2	1387	106.233	32.820	18	-46.0	-54.1	8.1	12.0	11.0	8.0			
3	2017	103.652	32.815	18	89.0	94.8	5.0	-38.0	-30.2	4.9			
4	2020	104.692	32.359	18	686.0	659.7	7.4	251.0	378.5	7.2	-80.0	-58.2	15.2
5	2031	102.372	31.000	20	163.0	140.3	6.7	-3.0	-10.5	6.6			
6	2033	103.090	30.064	20	-10.0	-8.7	4.4	-7.0	-17.6	4.1			
7	2037	105.071	31.081	20	-115.0	-183.8	6.2	26.0	37.7	6.0			
8	2049	103.640	30.624	20	-118.0	-132.1	6.0	120.0	105.4	5.8	-57.0	-55.1	13.5
9	2052	105.554	30.510	20	-42.0	-75.9	5.2	20.0	25.4	5.0			
10	BADN	110.350	31.049	1	-6.0	-13.1	3.0	3.0	2.9	2.9	0.0	2.8	5.2
11	BNSL	106.851	29.303	1	-10.0	-21.3	4.0	4.0	10.1	3.7	0.0	2.8	13.3
12	C125	104.817	34.381	21	1.0	5.8	8.5	10.0	23.9	8.5			
13	C127	105.295	34.027	20	1.0	8.2	8.9	14.0	39.3	9.0			
14	C140	104.078	34.365	21	11.0	7.9	8.9	7.0	11.4	8.7			
15	CHDU	104.064	30.639	1	-158.0	-179.4	4.9	117.0	100.9	4.8	-11.0	-22.9	4.8
16	CP02	102.151	30.066	22	7.0	12.0	4.6	4.0	-7.8	4.6			
17	CP11	102.871	29.291	26	-8.0	-4.8	4.6	-8.0	-10.2	4.6			
18	D066	108.999	34.974	5	3.0	-2.5	5.8	10.0	2.5	5.7			
19	D071	108.914	34.552	8	3.0	-4.0	6.4	14.0	2.2	6.4			
20	D072	108.233	34.496	5	-3.0	-3.3	5.6	10.0	3.8	5.6			
21	D073	107.580	34.433	8	6.0	-1.8	8.1	5.0	6.5	7.5			
22	D074	107.379	34.472	8	1.0	-0.8	5.1	3.0	7.8	5.1			
23	D077	108.194	34.302	6	0.0	-4.3	5.4	7.0	3.6	5.4			

DOI: 10.1038/NGEO636

24	D079	108.908	34.050	23	-6.0	-6.7	5.5	-2.0	1.7	5.5			
25	D080	108.157	34.110	6	2.0	-5.6	5.0	1.0	3.3	5.0			
26	D081	107.639	34.069	5	7.0	-4.6	5.7	3.0	5.5	5.6			
27	D082	107.294	34.088	8	1.0	-2.9	5.3	5.0	7.9	5.2			
28	DS08	104.953	33.460	20	5.0	13.7	9.7	53.0	74.6	9.7			
29	DS30	106.245	33.901	20	6.0	5.2	11.1	4.0	25.5	10.6			
30	F053	107.982	33.529	5	-6.0	-11.8	4.9	-2.0	2.5	4.9			
31	F262	106.322	33.063	18	-25.0	-21.1	8.0	23.0	17.1	8.0			
32	F277	105.781	32.826	18	-44.0	-19.7	8.4	46.0	61.7	8.3			
33	FDLH	108.015	29.816	1	-10.0	-21.5	3.6	6.0	8.6	3.5	0.0	4.2	7.5
34	FJHT	109.119	31.105	1	-8.0	-20.3	3.4	3.0	4.7	3.3	0.0	4.3	7.8
35	FJXL	109.444	30.667	1	-7.0	-17.1	3.1	2.0	4.7	2.9	0.0	3.7	5.6
36	G028	106.011	35.174	12	5.0	3.3	4.7	7.0	13.5	4.7			
37	G030	105.794	35.079	12	1.0	3.7	4.5	4.0	15.0	4.5			
38	G031	106.207	35.006	11	1.0	3.4	4.9	10.0	14.1	4.9			
39	G032	106.821	34.894	8	2.0	2.2	4.5	5.0	11.0	4.5			
40	G033	105.655	34.872	14	4.0	4.2	5.6	12.0	17.7	5.5			
41	G034	106.159	34.749	11	11.0	4.0	5.8	11.0	16.6	5.7			
42	G035	105.368	34.793	14	2.0	4.5	4.9	6.0	19.1	4.9			
43	G036	106.401	34.516	11	0.0	3.7	5.5	11.0	16.6	5.5			
44	G037	105.697	34.594	11	5.0	5.1	5.1	10.0	21.7	5.1			
45	G039	105.812	34.252	27	3.0	6.5	5.6	12.0	27.6	5.6			
46	G110	106.678	34.946	9	3.0	2.6	4.7	6.0	11.7	4.7			
47	G114	104.104	35.038	14	3.0	4.6	4.5	6.0	8.4	4.5			
48	G119	104.480	34.850	14	-1.0	4.5	4.8	14.0	13.3	4.8			

49	G120	104.940	34.714	18	6.0	4.6	4.7	13.0	18.9	4.7			
50	G121	104.915	34.467	17	3.0	5.4	5.0	13.0	23.1	5.0			
51	GUFU	110.748	31.341	1	-4.0	-11.6	2.8	1.0	2.2	2.7	0.0	2.5	4.9
52	GYAO	102.267	27.796	1	-2.0	-1.9	2.4	-2.0	-4.9	2.3	-3.0	-4.8	4.3
53	H001	106.509	33.915	18	11.0	2.2	5.0	1.0	18.9	5.0			
54	H002	105.814	33.891	27	0.0	9.0	5.5	22.0	37.9	5.4			
55	H003	105.306	34.108	27	6.0	7.6	5.5	22.0	36.0	5.4			
56	H004	106.924	33.617	5	-4.0	-6.6	5.1	5.0	10.2	5.1			
57	H005	105.595	33.697	5	3.0	12.3	5.4	31.0	54.0	5.4			
58	H006	105.285	33.780	28	3.0	10.5	5.9	27.0	53.2	5.9			
59	H007	106.155	33.340	18	-9.0	2.3	4.9	9.0	33.5	4.9			
60	H009	106.023	32.962	27	-23.0	-18.7	5.6	20.0	33.1	5.6			
61	H010	105.226	32.571	25	415.0	374.1	9.2	1005.0	814.4	9.2	299.0	406.7	8.9
62	H011	105.830	32.448	16	-195.0	-250.2	6.8	31.0	40.7	6.7			
63	H012	105.457	32.018	16	-243.0	-277.0	6.8	53.0	36.5	6.7			
64	H014	104.073	34.403	17	7.0	7.7	4.8	4.0	11.1	4.8			
65	H016	104.384	34.046	17	5.0	9.0	4.8	7.0	21.9	4.8			
66	H017	103.147	34.109	17	10.0	17.5	4.9	-3.0	-6.7	4.8			
67	H019	104.401	33.787	21	7.0	12.3	5.2	16.0	27.3	5.2			
68	H020	103.727	33.937	18	10.0	16.2	4.9	-4.0	3.2	4.8			
69	H021	104.824	33.423	18	11.0	15.3	6.2	44.0	69.2	6.2			
70	H022	104.625	33.001	23	49.0	54.5	6.2	67.0	80.0	6.1			
71	H024	104.226	33.228	7	31.0	39.2	5.3	10.0	23.8	5.3			
72	H025	103.435	32.931	21	62.0	77.5	6.4	-41.0	-34.0	6.4			
73	H026	102.991	33.571	21	25.0	34.1	5.4	-14.0	-18.9	5.4			

 DOI: 10.1038/NGEO636

74	H028	101.706	32.902	20	47.0	54.4	6.3	-29.0	-28.8	6.3			
75	H030	103.613	32.591	23	136.0	136.2	7.0	-48.0	-48.2	7.0			
76	H031	102.500	32.786	22	66.0	78.9	6.0	-46.0	-46.2	5.9			
77	H032	104.571	32.405	20	466.0	457.0	8.1	70.0	216.9	8.0			
78	H033	104.831	32.182	19	-1524.0	-1378.8	8.9	-143.0	-77.2	8.9	-662.0	-409.6	10.8
79	H034	103.732	32.361	24	209.0	213.7	6.6	-55.0	-58.7	6.6			
80	H035	104.444	31.802	4	-2379.0	-2178.7	8.6	481.0	535.9	8.5	-675.0	-738.9	10.9
81	H036	103.900	31.705	39	683.0	877.9	24.8	225.0	317.6	24.8			
82	H037	103.166	32.075	18	222.0	241.0	5.5	-113.0	-129.0	5.5			
83	H040	101.614	31.770	29	86.0	85.9	6.6	-25.0	-24.7	6.5			
84	H043	104.782	31.486	4	-304.0	-402.4	7.1	55.0	45.2	7.0			
85	H044	104.187	31.353	4	-983.0	-913.0	8.3	397.0	302.8	8.3	-123.0	-154.1	9.2
86	H046	102.670	31.850	30	237.0	222.2	6.8	-124.0	-107.5	6.8			
87	H047	102.096	31.466	19	156.0	138.0	6.2	-32.0	-33.8	6.2			
88	H048	104.441	31.157	4	-303.0	-398.8	5.7	99.0	114.7	5.7	-25.0	-23.0	5.6
89	H049	103.692	31.060	5	-1276.0	-1143.7	9.8	801.0	704.5	9.7	-216.0	-331.7	9.7
90	H050	103.145	31.008	30	640.0	586.8	8.2	-374.0	-196.5	8.2	-228.0	15.5	11.9
91	H052	101.866	30.949	18	84.0	74.9	5.9	2.0	-6.0	5.8			
92	H053	101.163	30.955	15	43.0	44.4	5.9	2.0	-4.2	5.8			
93	H054	100.750	31.297	15	37.0	41.2	5.5	-4.0	-6.2	5.4			
94	H058	104.077	30.732	13	-204.0	-230.3	7.3	140.0	123.0	7.2			
95	H060	103.410	30.415	13	-23.0	-32.8	6.7	5.0	2.7	6.5			
96	H061	102.840	30.252	6	-2.0	1.8	6.0	-17.0	-20.8	5.8			
97	H062	100.929	31.143	15	45.0	43.1	6.3	-7.0	-5.4	6.3			
98	H064	103.845	30.041	10	-24.0	-36.4	5.9	15.0	13.5	5.9			

DOI: 10.1038/NGEO636

99	H066	101.788	30.074	10	13.0	15.7	5.7	-9.0	-4.5	5.6			
100	H067	101.486	30.075	13	8.0	16.7	5.4	-1.0	-3.0	5.3			
101	H068	101.023	30.106	12	12.0	17.1	5.5	-4.0	-1.8	5.5			
102	H072	102.817	29.789	7	1.0	-4.0	5.2	-10.0	-14.4	5.2			
103	H073	102.290	29.848	9	9.0	4.4	5.6	-15.0	-10.0	5.6			
104	H074	101.558	29.846	11	8.0	10.8	5.3	1.0	-4.2	5.3			
105	H076	103.468	29.602	7	-8.0	-12.4	5.2	-3.0	-6.7	5.1			
106	H077	102.655	29.348	8	-1.0	-3.3	4.7	2.0	-10.5	4.6			
107	H078	102.080	29.688	9	3.0	4.2	5.5	-14.0	-8.1	5.5			
108	H081	103.261	29.228	7	-9.0	-7.4	5.4	-8.0	-8.2	5.4			
109	H082	102.439	29.263	10	4.0	-1.9	4.9	-2.0	-9.4	4.8			
110	H083	101.518	28.964	16	4.0	1.5	4.6	0.0	-5.2	4.6			
111	H087	102.767	28.955	8	-2.0	-3.9	5.0	-1.0	-8.5	4.9			
112	H088	103.978	28.605	7	2.0	-7.7	4.7	-1.0	-2.3	4.7			
113	H090	102.532	28.672	8	1.0	-2.8	4.8	4.0	-7.3	4.7			
114	H093	103.640	28.250	7	1.0	-5.0	6.6	-9.0	-3.9	6.0			
115	HCYT	106.367	30.106	1	-22.0	-40.5	3.5	8.0	16.2	3.4	0.0	5.3	4.3
116	HN02	104.585	30.317	14	-64.0	-84.5	6.1	34.0	37.7	6.1			
117	HN03	103.898	28.956	8	-8.0	-9.8	5.7	2.0	-2.3	5.5			
118	HN05	104.068	29.660	10	-21.0	-24.1	4.9	6.0	6.3	4.9			
119	JB08	108.086	35.058	5	1.0	-0.8	5.4	9.0	4.7	5.4			
120	JB23	106.681	33.116	30	-11.0	-22.6	5.2	8.0	8.6	5.2			
121	JB24	106.034	30.804	18	-37.0	-75.4	5.4	15.0	22.6	5.3			
122	JB27	105.379	35.141	15	6.0	3.6	4.8	13.0	14.7	4.8			
123	JB33	103.889	33.276	18	31.0	41.4	3.9	-4.0	1.1	3.8			

DOI: 10.1038/NGEO636

124	JB34	102.306	31.706	25	187.0	169.5	6.5	-66.0	-61.2	6.5	-20.0	18.6	7.2
125	JB35	101.497	30.495	12	30.0	32.4	6.1	-6.0	-2.1	6.1			
126	JB36	103.526	28.843	7	-3.0	-7.0	4.8	-3.0	-5.3	4.7			
127	JJML	106.254	29.182	1	-11.0	-21.0	3.2	6.0	10.1	3.1	0.0	1.6	5.0
128	JYAN	104.545	30.388	1	-71.0	-96.0	4.2	42.0	42.8	4.1	-1.0	-5.7	3.8
129	KAIY	102.112	27.882	1	-1.0	-1.7	2.5	-2.0	-4.9	2.4	2.0	-4.9	4.8
130	KXLJ	108.166	31.078	1	-14.0	-30.1	3.4	5.0	7.7	3.3	0.0	6.1	4.9
131	LESH	103.755	29.565	1	-12.0	-16.3	3.1	7.0	-1.3	3.0	-4.0	-13.6	4.8
132	LPFP	107.863	30.770	1	-15.0	-31.9	3.4	4.0	9.7	3.3	0.0	6.4	5.5
133	LUZH	105.414	28.872	1	-10.0	-16.0	2.7	4.0	6.9	2.6	1.0	-1.4	3.0
134	MAON	101.745	30.600	1	41.0	42.0	3.6	5.0	-2.4	3.5	-1.0	-2.6	4.2
135	MEIG	103.134	28.335	1	-3.0	-4.0	2.6	-1.0	-5.6	2.5	-3.0	-6.7	4.3
136	MYAN	104.726	31.440	1	-305.0	-410.4	5.4	66.0	58.3	5.4	-14.0	-18.5	4.9
137	NEIJ	105.119	29.620	1	-22.0	-32.3	3.4	11.0	14.2	3.3	0.0	-1.6	3.4
138	NR09	103.169	31.448	21	738.0	676.8	8.2	-392.0	-400.9	8.2			
139	PIXI	103.757	30.910	1	-563.0	-514.6	6.5	426.0	344.7	6.4	-81.0	-101.6	7.2
140	QIME	101.185	31.023	1	45.0	47.4	3.7	0.0	-5.0	3.6	1.0	4.3	4.0
141	QLAI	103.306	30.354	1	-15.0	-20.4	3.2	-3.0	-12.9	3.2	-28.0	-43.0	5.9
142	RCPL	105.350	29.534	1	-18.0	-29.6	3.2	9.0	13.2	3.2	0.0	-0.5	3.6
143	RENS	104.103	30.200	1	-51.0	-62.5	3.9	40.0	32.1	3.9	-5.0	-14.5	4.3
144	ROXI	104.434	29.458	1	-17.0	-22.7	3.4	10.0	7.5	3.3	-6.0	-6.9	8.0
145	SD07	102.438	31.143	17	226.0	190.5	11.2	-35.0	-26.1	11.2	12.0	0.6	9.1
146	TAGO	101.526	30.326	1	22.0	25.3	3.3	3.0	-2.3	3.2	-2.0	-3.6	4.2
147	WANZ	108.461	30.752	1	-10.0	-24.9	3.0	4.0	7.2	3.0	0.0	5.2	4.4
148	WARI	101.125	30.881	7	38.0	40.9	4.1	1.0	-3.5	4.1	-2.0	3.0	5.6

149	XIAA	108.986	34.178	1	-3.0	-5.9	2.2	1.0	1.7	2.1			
150	XICH	102.348	27.809	1	-1.0	-2.0	2.4	-2.0	-4.9	2.3	2.0	-4.9	4.6
151	YAAN	103.011	29.981	1	-4.0	-6.9	2.9	-8.0	-16.9	2.9	-16.0	-24.0	5.4
152	YBIN	104.597	28.798	1	-8.0	-12.1	2.9	3.0	2.5	2.8	-1.0	-4.6	4.2
153	Z040	103.677	32.043	18	310.0	370.8	7.2	-34.0	-94.5	7.1			
154	Z122	104.446	31.689	18	-945.0	-1061.6	9.3	439.0	302.3	9.1			
155	Z126	104.250	31.511	18	-1221.0	-1071.5	8.9	379.0	284.8	8.7	-204.0	-233.1	34.9
156	Z158	105.947	31.845	18	-100.0	-151.8	7.4	36.0	32.8	7.0			
157	Z246	103.578	30.866	20	-379.0	-433.6	8.1	366.0	346.1	7.9	-156.0	-140.8	35.3
158	ZHJI	104.546	31.006	1	-203.0	-275.3	4.9	73.0	83.9	4.8	-5.0	-8.6	4.3

* D is the number of days elapsed between the quake and the first postseismic GPS measurement at the site. E, Prd_E, Sig_E, N, Prd_N, Sig_N, U, Prd_U, Sig_U are the data entries, model predicted, and uncertainties for the east, north, and up components, respectively. Each uncertainty has been enlarged by adding $A^{1/4}$ to its original value, where A is the amplitude of observed coseismic displacement vector in millimeter.

backstory

Revealing ruptures

Zheng-Kang Shen and colleagues discovered an unusual cure for car-sickness while trying to understand the mechanics of fault deformation during the Wenchuan earthquake.

DR YANZHAO WANG

A crew member setting up GPS survey instruments at a mountain-top site after an hour-long hike. He is being watched by a local villager who helped carry survey equipment to the site.

What was the objective of the work?
We wanted to understand the mechanics of the fault rupture of the 2008 Wenchuan earthquake in China, which killed more than 80,000 people. The earthquake took place along the Longmen Shan fault. The rupturing of this fault reflects ongoing tectonic stress build-up that results from the eastward movement of the Tibetan plateau thrusting over the relatively stable Sichuan basin. We hoped that by measuring crustal deformation during and after the Wenchuan earthquake, we could better understand the geometry and extent of the fault rupture, as well as the mechanism of the earthquake and its associated tectonic processes.

Why did you choose this particular location for the fieldwork?
The earthquake chose the location for us, providing an exceptionally rare opportunity for study. Scientifically, few (if any) Earth scientists anticipated an event of this magnitude in this locality, even though the steep western margin of the Sichuan basin is known to be seismically active.

What sorts of data were you after?
We collected GPS data, together with radar data obtained from satellites. We used this data to measure crustal deformation resulting from the earthquake, and to determine fault geometry and slip distribution during the earthquake.

Did you encounter any difficulties?
We encountered most of our difficulties during the early phase of our fieldwork, which was carried out immediately after the quake. We came across roads that had been buried by landslides, collapsed bridges, vehicles hit by fallen rocks and a traffic accident in a congested road lined up with disaster-relief trucks. The living conditions were poor, with a lack of adequate food and water supplies at some camping grounds, and no power supply. Several of us suffered from altitude sickness while climbing mountains to survey sites. And there was the psychological trauma of seeing so much destruction.

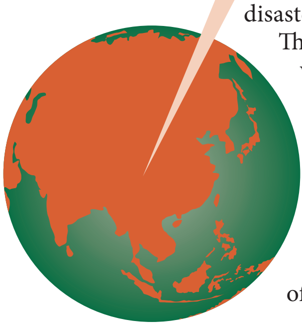

Did you have any encounters with dangerous animals?
One of our team members was stung by a hornet when working at a survey site. He had to run down a half-hour-long trail before being rushed to hospital.

Any low points?
On many occasions we were shocked by the scale of the devastation that the quake had caused. Among all the emotional lows, the one that stood out the most was when we had just finished a day of work and sought lodging assistance at a local government office. A lady in her thirties quietly arranged tents and meals for us. Afterwards, she asked, with a gentle and quiet voice: “Didn’t you know such a big one was coming?” We learnt later on that she had lost her husband in the earthquake.

What was the highlight of the expedition?
Having overcome all sorts of difficulties and hazards, we were elated when — two weeks after the quake — we had our instruments up and running at the first field site.

Did you learn anything new about yourself or your team members?
One of our crew members got car-sick while sitting in the back seat of a four-wheel-drive Toyota Land Cruiser, following a long drive along a treacherous rural road. With no other cure available, we put him in the front seat of a small and shaky pick-up truck, with tiny wheels and thin body parts. Bumping up and down, he sat in the car for the next several days, and never got car-sick again. We learnt that expensive and comfortable vehicles can still offer great discomfort, and that cheap uncomfortable vehicles are sometimes the best cure.

This is the Backstory to the work by Zheng-Kang Shen and colleagues, published on page 718 of this issue.